

# Membrane tension is a key determinant of bud morphology in clathrin-mediated endocytosis

Julian E. Hassinger<sup>1</sup>, George Oster<sup>2</sup>, David G. Drubin<sup>2</sup>, and Padmini Rangamani<sup>3</sup>

<sup>1</sup>Biophysics Graduate Group, University of California, Berkeley

<sup>2</sup>Department of Molecular and Cell Biology, University of California, Berkeley

<sup>3</sup>Department of Mechanical and Aerospace Engineering, University of California, San Diego

## Abstract

In clathrin-mediated endocytosis (CME), clathrin and various adaptor proteins coat a patch of the plasma membrane, which is reshaped to form a budded vesicle. Experimental studies have demonstrated that elevated membrane tension can inhibit bud formation by a clathrin coat. In this study, we investigate the impact of membrane tension on the mechanics of membrane budding by simulating clathrin coats that either grow in area or progressively induce greater curvature. At low membrane tension, progressively increasing the area of a curvature-generating coat causes the membrane to smoothly evolve from a flat to budded morphology, whereas the membrane remains essentially flat at high membrane tensions. Interestingly, at physiologically relevant, intermediate membrane tensions, the shape evolution of the membrane undergoes a *snaphrough instability* in which increasing coat area causes the membrane to “snap” from an open, U-shaped bud to a closed,  $\Omega$ -shaped bud. This instability is accompanied by a large energy barrier, which could cause a developing endocytic pit to stall if the binding energy of additional coat is insufficient to overcome this barrier. Similar results were found for a coat of constant area in which the spontaneous curvature progressively increases. Additionally, a pulling force on the bud, simulating a force from actin polymerization, is sufficient to drive a transition from an open to closed bud, overcoming the energy barrier opposing this transition.

## Author Contributions

J.E.H., G.O., and P.R. designed research. J.E.H. performed research. J.E.H., D.G.D., and P.R. analyzed data. J.E.H., G.O., D.G.D., and P.R. wrote the paper.

## Introduction

The plasma membrane of animal cells is under tension as a result of in-plane stresses in the bilayer and connections between the membrane and the underlying actomyosin cortex [1, 2]. In recent years, it has become increasingly clear that this membrane tension plays an important role in a variety of cellular processes, from cell motility [3] to controlling the balance of exocytosis and endocytosis [4, 5]. Of particular relevance to membrane-remodeling processes like endocytosis is the fact that membrane tension opposes deformations to the membrane by curvature-generating proteins [6]. In fact, despite estimates that membrane tension should have negligible impact on the energetics of membrane budding [7], recent experiments have shown that elevated membrane tension can inhibit clathrin-mediated endocytosis [8, 9].

Clathrin-mediated endocytosis (CME) is an essential cellular process in eukaryotes that is important for the intake of nutrients, signaling, and recycling the lipid and protein components of the plasma membrane [10]. During CME, over 60 different protein species act in a coordinated manner to invaginate a patch of the plasma membrane into a bud that subsequently undergoes scission, forming an internalized vesicle [11, 12]. CME is a classical example of a mechanochemical process, where a feedback between the biochemistry of the protein machinery and the mechanics of the plasma membrane and the actin cytoskeleton control endocytic patch topology and morphology [13, 14]. Figure 1 outlines the key mechanical steps of this process.

A critical step in CME is the assembly of a multicomponent protein coat that clusters cargo and bends the membrane into a budded morphology. Clathrin assembles into a lattice-like cage on the membrane with the assistance of adaptor proteins that directly bind lipids [11, 12]. This assembly is generally thought to act as a scaffold that imposes its spontaneous curvature on the underlying membrane [15]. Recent work suggests that other components of the coat can also contribute to membrane bending via scaffolding by F-BAR domains, amphipathic helix insertion into the bilayer, and adaptor protein crowding [7, 12, 16–18]. The contributions from each of these membrane bending mechanisms can be combined into a single measure of the curvature generating capability of the coat, or spontaneous curvature, with an effective strength that depends on its composition, density and area coverage [19, 20].

While coat proteins promote membrane budding, this process is opposed by the bending rigidity of the plasma membrane, membrane tension, turgor pressure, and cargo crowding [7, 8, 18, 21]. Crowding of cargo molecules on the outer leaflet of the plasma membrane opposes invagination of the membrane [7, 18, 22], though we can think of this effect as simply a negative contribution to the spontaneous curvature of the coat. In yeast, turgor pressure is believed to be the primary opposing force to endocytosis due to their especially high internal pressure [21, 23]. However, in mammalian cells, the turgor pressure is several orders of magnitude lower than that in yeast [24], and therefore contributes comparatively little as an opposing force to CME in these cells. Consequently, membrane bending resistance is generally thought to be the primary opposing force to membrane budding [7], though recent work has shown that membrane tension may also be a significant factor in this process [8, 9].

*In vivo*, elevated tension in combination with actin inhibitors causes clathrin-coated pits (CCPs) to exhibit longer lifetimes and increased the number of long-lived, presumably stalled, pits [8]. Under these conditions, open, U-shaped pits were found to be enriched as compared to closed,  $\Omega$ -shaped pits when visualized by electron microscopy [8, 25]. Similar observations have been made *in vitro* where purified coat proteins were able to substantially deform synthetic

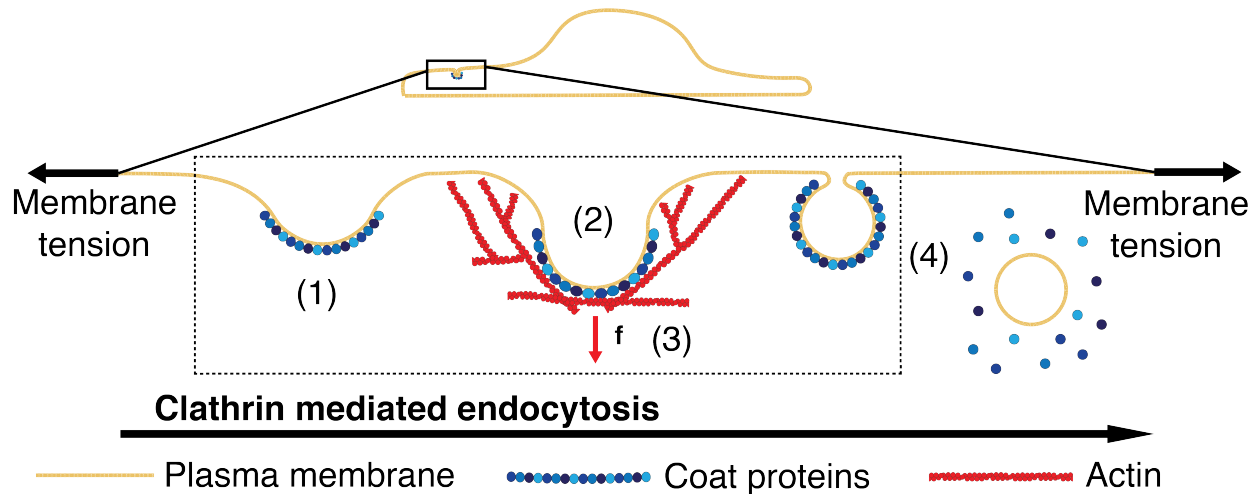


Figure 1: Schematic depiction of the key mechanical steps in clathrin-mediated endocytosis. (1) A multi-component **protein coat** forms on the **plasma membrane** and induces the membrane to bend inwards, forming a shallow pit. (2) As the coat grows, the membrane becomes deeply invaginated to form an open, U-shaped pit before constricting to form a closed,  $\Omega$ -shaped bud. The plasma membrane is under tension in physiological conditions, which opposes the budding process. (3) It is believed that **actin** polymerization provides a **force**,  $f$ , to facilitate these morphological changes, particularly at high membrane tensions [8]. (4) The bud subsequently undergoes scission to form an internalized vesicle and the coat is recycled. Our study is concerned with the impact of membrane tension on the morphological changes effected by the coat and actin polymerization, as indicated by the dashed box.

lipid vesicles under low tension but were stalled at shallow, U-shaped pits at a higher tension [9]. These studies demonstrated that elevated membrane tension can block the progression of CME and that actin polymerization seems to be necessary to overcome this opposition. However, these studies did not fully address the magnitude at which membrane tension becomes important relative to the curvature-generating capability of the coat nor the magnitude of applied force necessary to overcome elevated tension.

There are many challenges associated with elucidating the effect of membrane tension on CME using experimental techniques. The diffraction-limited size of CCPs ( $\sim 100$  nm) makes it currently impossible to directly image the morphology of the membrane in a live cell. The regularity of yeast CME has allowed for the visualization of time-resolved membrane shapes in this organism via correlative fluorescence and electron microscopy [26, 27]. However, the wide distribution of CCP lifetimes in mammalian cells [28, 29] makes this approach difficult in these cells. Additionally, current techniques are only capable of measuring global tension [2, 30, 31]. Due to these limitations, it is impossible to determine how the local membrane tension at a given CCP impacts the progression of membrane deformation.

On the other hand, mathematical modeling has provided insight into various aspects of membrane deformation in CME. For example, Liu et al. showed that a line tension at a lipid phase boundary could drive scission in yeast [13, 32], while Walani et al. showed that scission could be achieved via snapthrough transition at high membrane tension [33]. These studies and others [23, 34, 35] have demonstrated the utility of membrane modeling approaches for studying CME, though none have systematically explored the effect of varying membrane tension on the morphological progression of membrane budding.

Since an endocytic patch is a small region ( $\sim 100$  nm [36, 37]) that is connected to the larger cell membrane, we reasoned that plasma membrane tension is likely to be key determinant of the bud morphology in CME. In this study, we develop a modeling framework to investigate the impact of membrane tension on budding processes like CME. This model accommodates heterogeneous membrane composition through the spontaneous curvature term. Using this model we show that membrane tension, in conjunction with the coat spontaneous curvature and coat coverage area, determines the morphology of the CCP. We also identify the circumstances in which CCPs traverse a *snaphthrough instability* to transition from U-shaped buds to  $\Omega$ -shaped buds. Finally, we show that an externally applied force can mediate this transition.

## Model development

We model the lipid bilayer as a thin elastic shell. The bending energy of the membrane is modeled using the Helfrich-Canham energy, which is valid for radii of curvatures much larger than the thickness of the bilayer [19]. Since typical endocytic patch radii of curvatures are  $\approx 50$  nm [36, 37], application of this model provides a valid representation of the shapes of the membrane. Further, we assume that the membrane is at mechanical equilibrium at all times. Because clathrin-mediated endocytosis occurs over a timescale of tens of seconds [8, 28, 29, 38], the membrane has sufficient time to attain mechanical equilibrium at each stage [13, 23]. We also assume that the membrane is incompressible because the energetic cost of stretching the membrane is high [39]. This incompressibility constraint is implemented using a Lagrange multiplier (see Section 1 SOM for details). Finally, for simplicity in the numerical simulations,



we assume that the endocytic pit is rotationally symmetric (Figure S1).

Since one of the key features of CME is coat-protein association with the plasma membrane, we model the strength of curvature induced by the coat proteins with a spontaneous curvature term ( $C$ ). The spontaneous curvature represents an asymmetry across the membrane that favors bending in one direction over the other with a magnitude equal to the inverse of the preferred radius of curvature. Classically, this was used to represent differences in the lipid composition (i.e. head group size and tail length/number) of the two monolayers that would cause the membrane to bend [19]. In our case, the spontaneous curvature represents the preferred curvature of the coat proteins bound to the cytosolic face of the membrane, consistent with its usage in other studies [6, 23, 33, 40, 41].

Our model reflects the fact that the clathrin coat covers a finite area and that this region should have different physical properties (e.g. spontaneous curvature, bending rigidity) than the surrounding membrane. Heterogeneity in the spontaneous curvature and bending rigidity is accommodated by using a local rather than global area incompressibility constraint [42, 43]. This allows us to simulate a clathrin coat by tuning the size, spontaneous curvature, and rigidity of the “coated” region relative to the bare membrane.

We use a modified version of the Helfrich energy that includes a spatially-varying spontaneous curvature,  $C(\theta^\alpha)$  [33, 40, 42],

$$W = k(H - C(\theta^\alpha))^2 + \bar{k}K, \quad (1)$$

where  $W$  is the energy per unit area,  $k$  is the bending modulus,  $\bar{k}$  is the Gaussian bending modulus,  $H$  is the local mean curvature, and  $K$  is the local Gaussian curvature.  $\theta^\alpha$  denotes the surface coordinates where  $\alpha \in \{1,2\}$ . Note that this energy function differs from the standard Helfrich energy by a factor of 2, with the net effect being that our value for the bending modulus,  $k$ , is twice that of the standard bending modulus typically encountered in the literature. The resulting “shape equation” for this energy functional is

$$\underbrace{k\Delta(H - C) + 2k(H - C)(2H^2 - K) - 2kH(H - C)^2}_{\text{Elastic Effects}} = \underbrace{p + 2\lambda H}_{\text{Capillary effects}} + \underbrace{\mathbf{f} \cdot \mathbf{n}}_{\text{Force due to actin}}, \quad (2)$$

where  $\Delta$  is the surface Laplacian,  $p$  is the pressure difference across the membrane,  $\lambda$  is interpreted to be the membrane tension,  $\mathbf{f}$  is a force per unit area applied to the membrane surface, and  $\mathbf{n}$  is the unit normal to the surface [33, 42]. In this model,  $\mathbf{f}$  represents the applied force exerted by the actin cytoskeleton; this force need not necessarily be normal to the membrane.

A consequence of heterogeneous protein-induced spontaneous curvature and externally applied force is that  $\lambda$  is not homogeneous in the membrane [40, 42]. The spatial variation in  $\lambda$  is accounted for as

$$\underbrace{\lambda_{,\alpha}}_{\text{Gradient of surface pressure}} = \underbrace{-2k(H - C)\frac{\partial C}{\partial x^\alpha}}_{\text{protein-induced variation}} - \underbrace{\mathbf{f} \cdot \mathbf{a}_\alpha}_{\text{force induced variation}}, \quad (3)$$

where  $(\cdot)_{,\alpha}$  is the partial derivative with respect to the coordinate  $\alpha$  and  $\mathbf{a}_\alpha$  is the unit tangent in the  $\alpha$  direction.  $\lambda$  can be interpreted as the surface tension [40, 44], and in our case is also affected by the tangential components ( $\mathbf{a}_\alpha$ ) of the force due to the actin cytoskeleton. The complete derivation of the boundary value problem and simulation details are given for axisymmetric coordinates in the SOM.

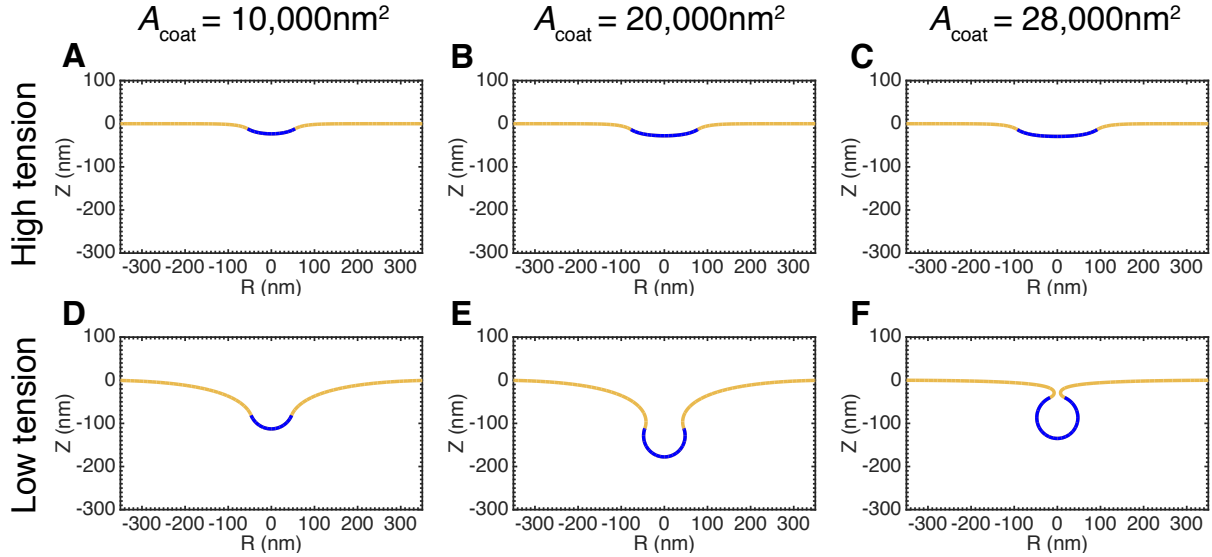


Figure 2: Profile views of membrane morphologies generated by simulations where the area of a **curvature-generating coat** progressively increases, covering more of the **bare membrane**. Simulations were performed for both high and low values of membrane tension. The curvature-generating capability, or spontaneous curvature, of the coat is set at  $C_0 = 0.02 \text{ nm}^{-1}$ , corresponding to a preferred radius of curvature of 50 nm. **(C)** High membrane tension,  $\lambda_0 = 0.2 \text{ pN/nm}$ . The membrane remains nearly flat as the area of the coat increases. **(D-F)** Low membrane tension,  $\lambda_0 = 0.002 \text{ pN/nm}$ . Addition of coat produces a smooth evolution from a flat membrane to a closed bud.

## Results

### Membrane tension inhibits bud formation by curvature-generating coats

In order to understand how membrane tension affects the morphology of a coated membrane, we performed simulations in which a curvature-generating coat “grows” from the center of an initially flat patch of membrane. For simplicity, the spontaneous curvature was set to be constant,  $C_0 = 0.02 \text{ nm}^{-1}$ , in the coated region with a sharp transition at the boundary between the coated and bare membrane (implemented via hyperbolic tangent functions, Figure S2). The membrane tension was varied by setting the value of  $\lambda$  at the boundary of the membrane patch, which corresponds to the tension in the surrounding membrane reservoir. Figure 2 shows the morphology of the membrane under low and high tension conditions for these “coat-growing” simulations, in the absence of any force from actin assembly (i.e  $\mathbf{f} = 0$ ).

High membrane tension (0.2 pN/nm) inhibits deformation of the membrane by the protein coat (Figure 2C). Even as the area of the coated region ( $A_{\text{coat}}$ ) increases, the membrane remains nearly flat. In fact, the size of the coated region can grow arbitrarily large without any substantial deformation (Figure S3). The spontaneous curvature of the coat is simply unable to overcome the additional resistance provided by the high membrane tension.

In contrast, at low membrane tension (0.002 pN/nm), the protein coat is able to substantially

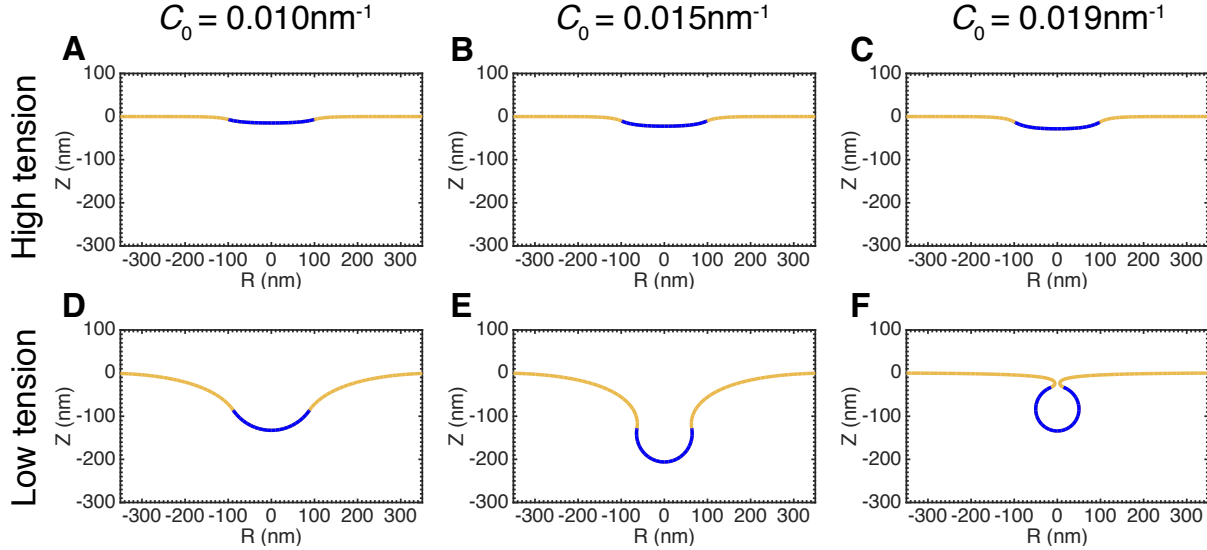


Figure 3: Membrane profiles for simulations with a constant coat area in which the spontaneous curvature of the **coat** progressively increases. The area of the coat is  $31,416 \text{ nm}^2$ , the approximate surface area of a clathrin-coated vesicle [37]. **(C)** High membrane tension,  $\lambda_0 = 0.2 \text{ pN/nm}$ . The membrane remains nearly flat with increasing spontaneous curvature. **(D-F)** Low membrane tension,  $\lambda_0 = 0.002 \text{ pN/nm}$ . Increasing the spontaneous curvature of the coat produces a smooth evolution from a flat membrane to a closed bud.

deform the membrane from its initial, flat morphology to a closed bud (Figure 2D-F). Increasing the coat area causes a smooth evolution from a shallow to deep U-shape to a closed,  $\Omega$ -shaped bud. We stopped the simulations when the membrane is within 5 nm of touching at the neck, at which point bilayer fusion resulting in vesicle scission is predicted to occur spontaneously [32]. These morphological changes are similar to those observed in clathrin-mediated endocytosis [37] and do not depend on the size of the membrane patch (Figure S4).

Can increasing the spontaneous curvature of the coat overcome tension-mediated resistance to deformation? To answer this question, we performed simulations in which the spontaneous curvature of the coat increases while the area covered by the coat remains constant at approximately the surface area of a typical clathrin coated vesicle [37]. As before, high membrane tension (Figure 3C) prevents deformation of the membrane by the coat. Even increasing the spontaneous curvature to a value of  $0.04 \text{ nm}^{-1}$ , corresponding to a preferred radius of curvature of 25 nm and twice the value used in the simulations in Figure 2, does not produce a closed bud (Figure S5). In the case of low membrane tension (Figure 3D-F), a progressive increase in the coat spontaneous curvature causes a smooth evolution from a shallow to deep U-shape to a closed,  $\Omega$ -shaped bud.

The similarity between the membrane morphologies in Figures 2 and 3 suggests that the interplay between spontaneous curvature, coat area and membrane tension is more important than the exact timing of coat protein arrival relative to the bending of the membrane, particularly in the absence of other membrane bending mechanisms. In the results that follow, we

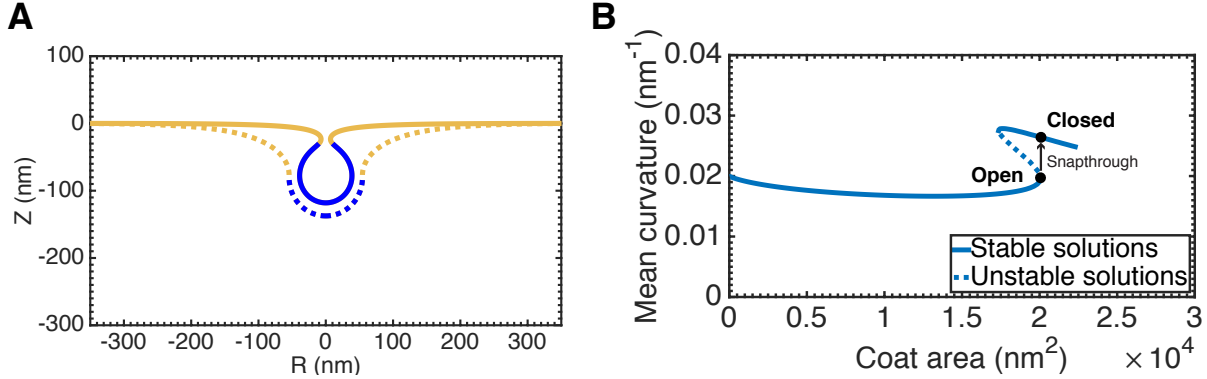


Figure 4: A snapthrough instability exists for increasing coat area at intermediate, physiologically relevant [45], membrane tensions,  $\lambda_0 = 0.02$  pN/nm. **(A)** Membrane profiles showing bud morphology before (dashed line,  $A_{\text{coat}} = 20,065$  nm<sup>2</sup>) and after (solid line,  $A_{\text{coat}} = 20,105$  nm<sup>2</sup>) addition of a small amount of area to the coat. **(B)** Mean curvature at the tip of the bud as a function of the coat area. There are two stable branches of solutions of the equilibrium membrane shape equations. The lower branch consists of open, U-shaped buds while the upper branch consists of closed,  $\Omega$ -shaped buds. The dashed portion of the curve indicates “unstable” solutions that are not accessible by simply increasing and decreasing the area of the coat. The marked positions on the curve denote the membrane profiles shown in (A). The transition between these two shapes is a snapthrough, in which the bud “snaps” closed upon a small addition to area of the coat.

performed simulations with increasing coat area, though the results are equally applicable to the case of increasing coat spontaneous curvature.

### Transition from U- to $\Omega$ -shaped buds occurs via instability at intermediate membrane tensions

Experimentally measured membrane tensions in live mammalian cells typically fall between the high and low tension regimes presented in Figures 2 and 3 [45]. Figure 4 shows the result of a coat-growing simulation with membrane tension at an intermediate value of 0.02 pN/nm. As in the low membrane tension case, increasing the area of the coat causes substantial deformation of the membrane. However, there is no longer a smooth transition from an open bud to a closed bud. Figure 4A shows a bud just before (dashed line) and after (solid line) a small amount of area is added to the coat. Evidently, this small change causes the bud to “snap” closed to an  $\Omega$ -shaped morphology. This situation is known as a *snaphthrough instability*, and similar instabilities have been observed in other recent membrane modeling studies [23, 33]. We emphasize that these are two equilibrium shapes of the membrane, and the exact transition between these states (i.e. intermediate unstable shapes and timescale) is not modeled here.

To better visualize why this sharp transition should occur, Figure 4B shows the mean curvature at the tip of the bud as a function of the area of the coat. In comparison to the high and low membrane tension cases (Figure S6), there are two branches of stable solutions. The lower and upper branches represent “open” and “closed” morphologies of the bud, respectively.

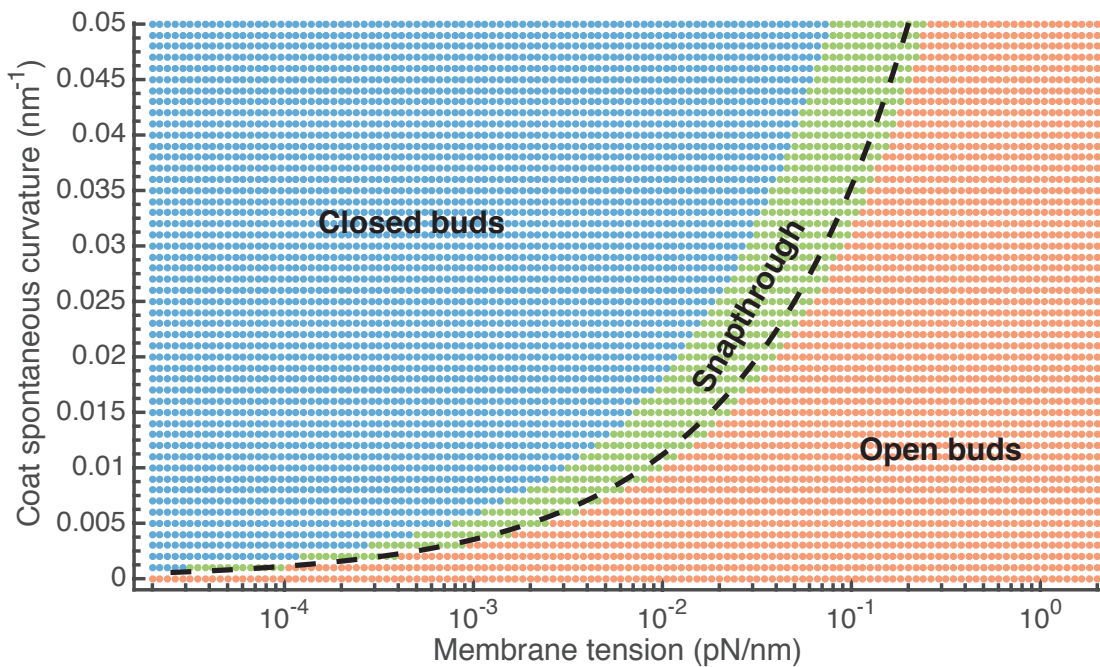


Figure 5: Coat spontaneous curvature ( $C_0$ ) vs. membrane tension ( $\lambda_0$ ) phase diagram. The shape evolution of the budding process depends on both the membrane tension and coat spontaneous curvature. Each dot represents a coat “growing” simulation performed with the specified values for edge membrane tension and coat spontaneous curvature. The dots are colored according to the final shape of the membrane: **Blue** denotes closed,  $\Omega$ -buds, **Red** denotes open, U-shaped pits, and **Green** are situations in which closed buds are obtained via a snaphrough transition. The snaphrough solutions cluster about the dotted line,  $Ves = 1$ , which separates the “high” and “low” membrane tension regimes (see main text).

The marked solutions show the location of the two morphologies depicted in Figure 4A. The open bud in Figure 4A is at the end of the open bud solution branch, so any addition of area to the coat necessitates that the membrane adopt a closed morphology. A similar snaphrough, albeit with a less severe morphological transition, occurs when the bending rigidity of the coated region is increased [46] relative to the bare membrane (Figure S7).

Over what ranges of tension and spontaneous curvature does this snaphrough transition occur? In order to understand the nature of the transition between low and high membrane tension regimes, we performed simulations over several orders of magnitude of the membrane tension ( $10^{-4}$  to 1 pN/nm), encompassing the entire range of measured physiological tensions [45] (Figure S8). We then performed these simulations over a range of spontaneous curvatures of the coat (0 to  $0.05 \text{ nm}^{-1}$ ) corresponding to preferred radii of curvature from 20 nm and up. Based on the results, we constructed a phase diagram summarizing the observed morphologies (Figure 5). Each dot in the diagram represents one simulation at the corresponding values of membrane tension and coat spontaneous curvature. The **blue** region denotes a smooth evolution

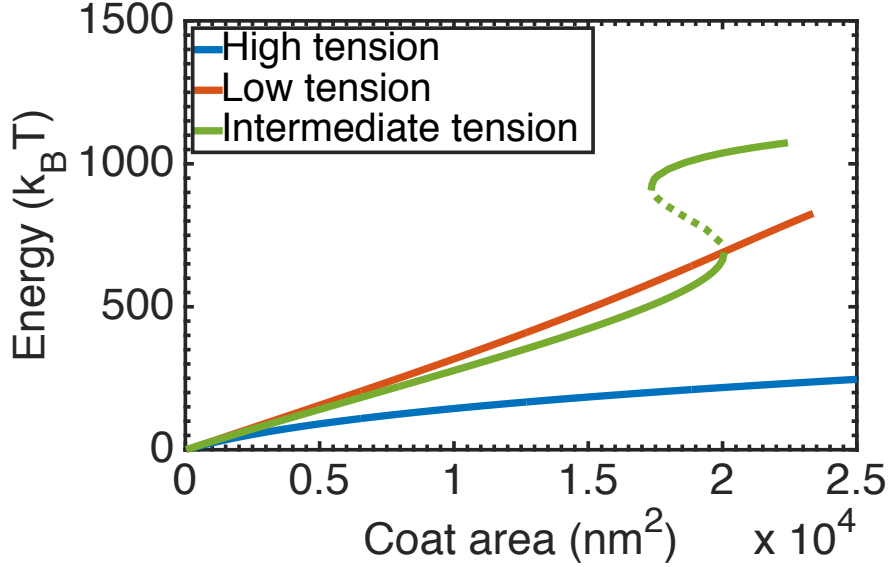


Figure 6: An energy barrier opposes coat closing at the instability. The energy input necessary to deform the membrane is plotted as a function of the area of the coat for three values of membrane tension. **High membrane tension**,  $\lambda_0 = 0.2$  pN/nm. **Low membrane tension**,  $\lambda_0 = 0.002$  pN/nm. **Intermediate membrane tension**,  $\lambda_0 = 0.02$  pN/nm. At the intermediate membrane tension, there is an energy difference of over  $100 k_B T$  between the U- and  $\Omega$ -shaped buds. This energy barrier could prevent the transition from U- to  $\Omega$ -shaped buds if the polymerization energy of the coat is insufficient to overcome the barrier.

to a closed bud, the **red** region represents a failure to form a closed bud, and **green** region indicates a snapthrough transition from an open to a closed bud. This phase diagram clearly shows that the distinction between “low” and “high” membrane tension conditions depends on the magnitude of the spontaneous curvature of the coat.

These results can be understood by comparing the spontaneous curvature of the coat to the membrane tension and bending rigidity via the dimensionless quantity,  $Ves = \frac{C_0}{2} \sqrt{\frac{\kappa}{\lambda}}$ , hereafter termed the *vesiculation number*. The dashed line in Figure 5 corresponds to  $Ves = 1$ , which bisects the low ( $Ves > 1$ ) and high tension ( $Ves < 1$ ) results. The snapthrough results cluster about this line, marking the transition region between the high and low tension cases. Importantly, this demonstrates that the preferred radius of curvature of the coat,  $1/C_0$ , must be smaller than the “natural” length scale of the membrane,  $\frac{1}{2} \sqrt{\kappa/\lambda}$  [23], for the coat to be capable of producing a closed bud in the absence of other mechanisms of curvature generation.

### A large energy barrier accompanies the instability

What is the energy cost that is associated with membrane deformation? For the budding process to proceed from an open, shallow invagination to a closed bud, the free energy gain from the assembly of the coat (*i.e.* the binding energy of the protein-protein and protein-lipid interactions) must exceed the energy necessary to deform the membrane [9, 47]. To examine

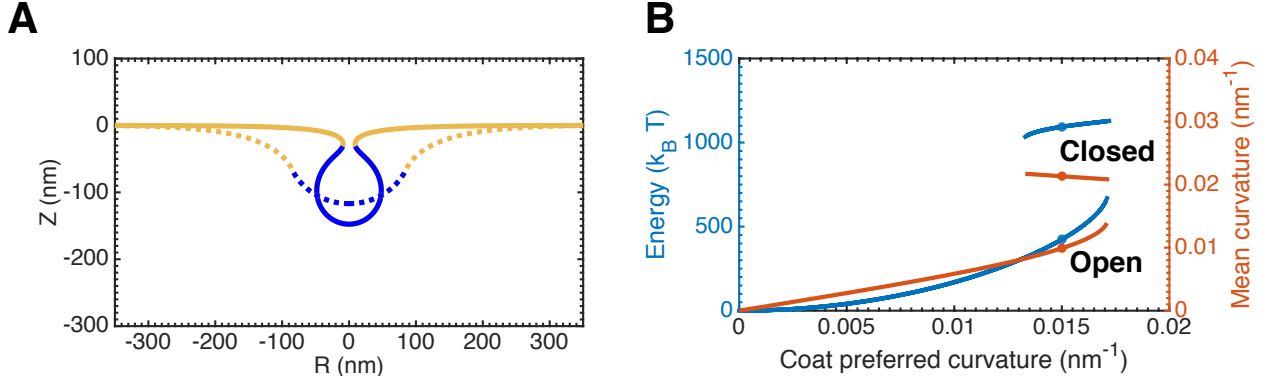


Figure 7: The instability and energy barrier are present at intermediate tensions for increasing spontaneous curvature  $C_0$ ,  $\lambda_0 = 0.02 \text{ pN/nm}$ ,  $A_{\text{coat}} = 31,416 \text{ nm}^2$ . **(A)** Membrane profiles showing U-shaped (dashed line) and  $\Omega$ -shaped (solid line) solutions at an identical coat spontaneous curvature,  $C_0 = 0.015 \text{ nm}^{-2}$ . **(B)** Energy necessary to deform the membrane and mean curvature at the tip of the bud as a function of the spontaneous curvature of the coat. The two stable branches are open (lower) and closed (upper) buds. There is a substantial energy barrier ( $> 100 k_B T$ ) between the U- and  $\Omega$ -shaped buds.

this requirement, we calculated the energy needed to bend the membrane at the low, high, and intermediate membrane tensions as a function of the coat area (Figure 6). Details of the calculation can be found in Section 3 of the SOM. Since the energy is proportional to the square of the mean curvature (Eq. S11), it is not surprising that the highly curved, budded morphologies in the low membrane tension case cost more energy to produce than the flat morphologies at high tension. Indeed, the main contribution to the energy in the low tension case is the bending rigidity (Figure S9C), whereas the energy cost from tension and bending rigidity are comparable at high tension (Figure S9A).

In the case of intermediate membrane tension, we again see the two stable solution branches corresponding to the open and closed bud morphologies. Notably, the major opposing force is bending rigidity of the membrane and resistance from membrane tension contributes only a minor amount to the overall energy (Figure S9B), consistent with previous estimates [7]. Though the energy for the open buds in the intermediate case is similar to that in the low tension case, there is a large ( $> 100 k_B T \approx 250 \text{ kJ/mol}$ ) energy barrier between the open and closed bud morphologies. Thus, *if* the polymerization energy of the coat is insufficient to reach the upper solution branch, then we should expect to observe “stalled” buds in an open, U-shaped configuration at intermediate membrane tensions in the absence of other mechanisms of curvature generation. It should be noted that the exact magnitude of the energy necessary to deform the membrane, along with the energy barrier at this intermediate membrane tension, depends on the bending rigidity,  $k_0$ , of the membrane (see Equation S43).

We observed a similar result when the spontaneous curvature was varied for a constant coat area. Figure 7A shows representative open (dashed line) and closed (solid line) membrane morphologies at identical spontaneous curvatures. Figure 7B plots the energy necessary to deform the membrane and mean curvature of the bud tip as a function of the spontaneous

curvature of the coat, and the marked points denote the solutions shown in Figure 7A. There are again two branches of solutions to the equilibrium equations with the lower branch representing open buds and the upper branch closed buds. Substantially more energy ( $> 100 k_B T$ ) is required to deform the membrane into closed buds as compared to the open buds at identical coat spontaneous curvatures.

## A pulling force can mediate the transition from a U- to $\Omega$ -shaped bud

What mechanisms of force generation enable the cell to overcome the energy barrier? Experiments have demonstrated that CME is severely affected by a combination of elevated tension and actin inhibition [8, 28]. To examine whether a force from actin polymerization is sufficient to induce a transition from open to closed bud morphologies, we modeled the force from actin polymerization as a “pulling” force on the bud as shown in Figure 1. It should be noted that the ultrastructure of the actin cytoskeleton at CME sites in live cells, and hence the exact orientation of the applied force, is currently unknown. This merely represents a candidate orientation analogous to the force from actin polymerization in yeast CME [27].

We find that a pulling force of less than 10 pN is sufficient to drive the membrane from an open to closed configuration (Figure 8). Figure 8A demonstrates that a downward pulling force on the coated region is sufficient to drive a transition from an open U-shaped bud to an  $\Omega$ -shaped bud. Then, while holding the bud at a prescribed depth, area can be added to the coat, further closing the bud (Figure 8B). The force required to pull the bud (Figure 8A) and then maintain its position (Figure 8B) is less than 10 pN (Figure S10), well within the capability of a polymerizing actin network [48].

Once again, there are two branches of solutions with increasing coat area, as seen in Figures 8C and 8D which plot the mean curvature of the tip of the bud and the energy necessary to deform the membrane, respectively. However, these solution branches are now fundamentally different as  $\mathbf{f} = 0$  pN in the **lower branch** (identical to Figure 4), while  $\mathbf{f} \approx 6$  pN in the **upper branch** (Figure S10B). There is a substantial energy barrier between the two solution branches ( $\approx 350 k_B T$ ), though this could be overcome by an actin network composed of a few hundred actin monomers, assuming an energy efficiency of  $\sim 5\%$  [48]. This is quite reasonable given recent measurements in yeast, in which the number of actin monomers was estimated to be on the order of thousands [27, 49]. An effective “pinching” force, as suggested by the results of Collins et al. [36], is also sufficient to induce the transition from U- to  $\Omega$ -shaped buds (Figure S11). These results demonstrate that the actin cytoskeleton can overcome an energy barrier to forming a closed bud at physiological membrane tensions in mammalian cells.

## Discussion

Despite our extensive knowledge of the protein machinery and dynamics of CME [38], we do not completely understand how membrane tension influences this process. An important challenge in understanding the role of membrane tension is that it is difficult to measure and to interpret the effects of membrane tension. Traditionally, membrane tension measurements on live cells have been performed by measuring the force required to hold a tube pulled from the plasma membrane [30, 50]. The tension obtained from this measurement is a combination of the in-plane tension in the membrane as well as the energy from membrane-to-cortex attachments (MCA)



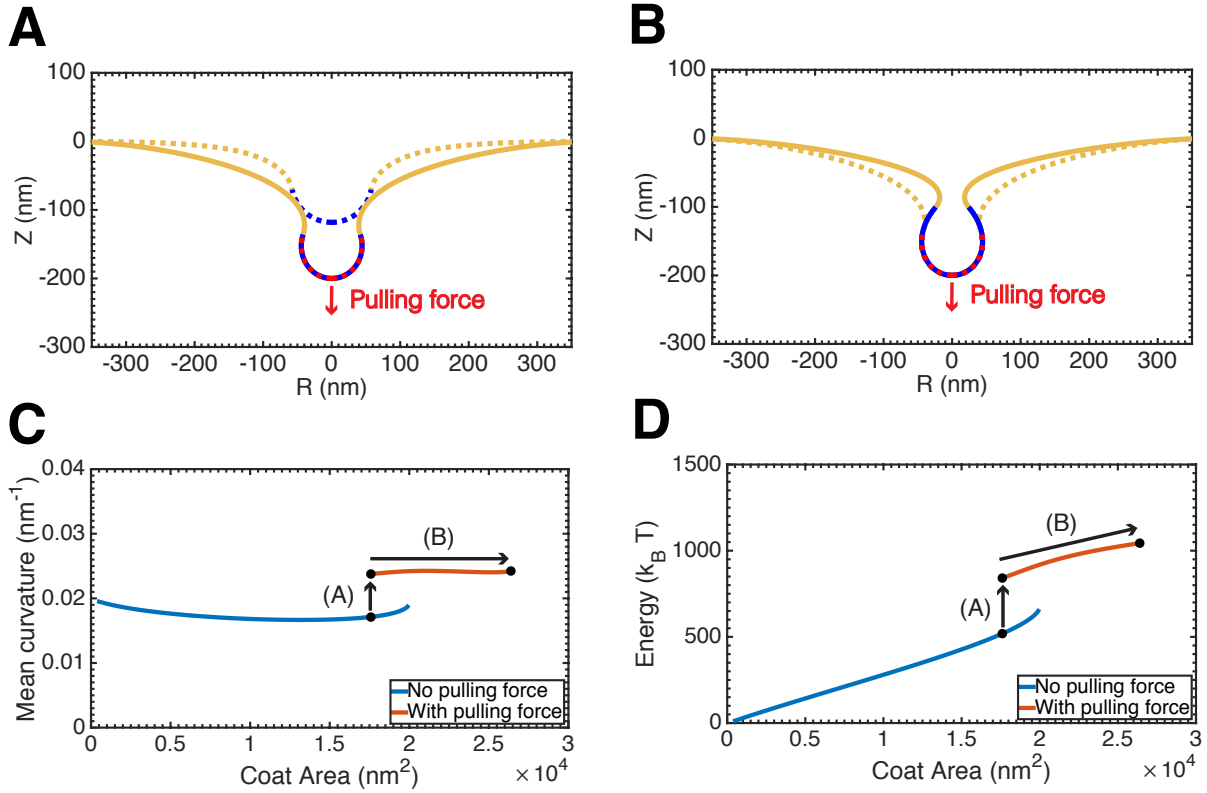


Figure 8: A pulling force can mediate the transition from a U- to  $\Omega$ -shaped bud. **(A)** At a constant coat area,  $A_{\text{coat}} = 17,593 \text{ nm}^2$ , a **pulling force** (red dash) localized to the coat drives the shape transition from a U-shaped (dashed line) to  $\Omega$ -shaped bud (solid line). **(B)** The bud can be closed further (solid line) by increasing the area of the coat while the **pulling force** holds the tip of the bud at  $Z = -200 \text{ nm}$ . **(C)** Mean curvature at the tip of the bud as function of the coat area. The pulling force bridges the two solution branches. **(D)** Energy to deform the membrane as a function of the coat area. The pulling force provide the energy input to reach the upper solution branch. The black arrows in (C) and (D) indicate the direction of the simulations in (A) and (B) with the marked points indicating the solutions corresponding to the shown membrane profiles.

[2, 24]. Whether the MCA impacts the effective tension felt at CCPs is not clear, but because the actin cortex is not homogeneous throughout the cell [51] and can act as a diffusion barrier to lipids and transmembrane proteins [52, 53], endocytic pits in different regions of cells might be subject to different effective membrane tensions.

In this study, we investigated the role of membrane tension in governing the morphological landscape of CME and found that a combination of membrane tension and protein-induced spontaneous curvature governs the morphology of the endocytic pit (Figures 2, 3). Additionally, we found that at intermediate membrane tensions, the bud must go through a snapthrough to go from an open to closed configuration (Figure 4). The full range of bud morphologies for different values of membrane tension and spontaneous curvature is shown in Figure 5. A key result from this work is that the vesiculation number can be used to identify the regime of tension and curvature-mediated effects that separates the closed and open bud morphologies. Finally, we found that a force modeling actin polymerization in CME can mediate the transition between open and closed buds at physiologically relevant membrane tensions. We believe these can results can explain the observations of a number of recent experimental studies.

There has been conflicting evidence as to whether actin is an essential component of the endocytic machinery in mammalian cells [8, 25, 28]. This is in contrast to the situation in yeast where actin assembly is absolutely required for productive CME, presumably to counteract the substantial turgor pressure in this organism [21, 23]. A hypothesis that follows from our work is that the membrane tension in a particular cell type should determine whether actin polymerization is required for productive CME.

This hypothesis is consistent with experimental observations. Boulant et al. found that treatment with jasplakinolide left CME unaffected in typical conditions, but the same treatment had a severe inhibitory effect in cells subjected to hypoosmotic shock or mechanical stretching [8]. One interpretation of this result is that physiological membrane tension was initially in the “low” tension regime, and the increase in membrane tension caused by the hypoosmotic shock or stretching pushed the membrane tension to intermediate or high values in which the coat alone is insufficient to produce closed buds. The observed overabundance of U-shaped, presumably stalled, pits [8] is consistent with a situation in which the membrane tension is in the snapthrough regime and the free energy of coat assembly is unable to overcome the energy barrier necessary to deform the membrane into a closed bud shape. Thus, under conditions of hypoosmotic shock it seems that a force exerted by the actin cytoskeleton, as in Figure 8, is necessary to overcome the energy barrier required to form a closed bud.

Avinoam et al. found that the size of the coat does not change substantially during membrane deformation in CME [37]. This is in contrast to the canonical view that the clathrin coat should directly impose its preferred curvature on the underlying membrane [15]. There are two possible explanations for this observation in the context of our study. One is that the membrane tension is too high for the coat to deform the membrane, so that other mechanisms of curvature generation (e.g. actin polymerization or BAR domain proteins) are necessary to remodel the membrane. The second is that the coat undergoes a “maturation” process that progressively increases its capability to bend the membrane, and hence its spontaneous curvature, as in Figure 3.

In principle, we can distinguish between these two possibilities by measuring the membrane tension in the SK-MEL-2 cell type used in the study. Calculating the vesiculation number could then be used to predict whether the clathrin coat alone is sufficient to produced closed buds or if another membrane remodeling mechanism (e.g. actin assembly) is necessary. Preliminary tether

pulling measurements on this cell line yielded tether forces of  $38 \pm 12$  pN [**unpublished data**], corresponding to a membrane tension of  $\lambda_0 = 0.12 \pm 0.08$  pN/nm, assuming a value of  $k = 320$  pN·nm. This value of membrane tension falls within the high tension or snapthrough regime for a wide range of spontaneous curvatures, indicating that additional facilitators of curvature generation may be necessary to produce closed buds in this cell type. This is consistent with the observation that actin inhibition causes substantial defects in CME in this cell type [28]. Thus, it is possible that the findings of Avinoam et al. [37] might be specific to the cell type used and in particular on the typical membrane tension of that cell line.

By reconstituting clathrin coat formation from purified components, Saleem et al. measured the polymerization per unit area of a clathrin coat to be  $1.0 \pm 0.5 \times 10^{-4} \text{ N} \cdot \text{m}^{-1} \approx 2.5 \pm 1.3 \times 10^{-2} k_B T \cdot \text{nm}^{-2}$  [9]. This energy is sufficient to produce a closed bud at low membrane tensions for the value of the bending modulus,  $k = 104 \pm 40$  pN·nm, of the synthetic lipid membranes used in this study. This is consistent with the gross membrane deformation and formation of closed buds observed in hypertonic, low membrane tension conditions [9]. However, this energy would be insufficient to bridge the energy barrier to coat closing at intermediate membrane tensions. This suggests that this energy barrier might be physiologically relevant. Additionally, we can calculate the vesiculation number for the membrane tensions ( $\approx 0.5 - 3$  pN/nm) set by micropipette aspiration to be less than 1 over a wide range of spontaneous curvatures, indicating the high membrane tension regime. This is consistent with the shallow buds observed in isotonic conditions. One result that our model cannot explain is the lack of any clathrin assembly observed under hypotonic conditions [9]. It is possible that at extremely high membrane tensions the coat is simply unable to stay bound to the membrane at the extremely flat morphology that would be expected. Saleem et al. also constructed a theoretical phase diagram comparing the resultant membrane shapes as a function of membrane tension and the polymerization energy of the coat that seems to well explain their observations [9]. However, their model is limited in that it explicitly assumes that the underlying membrane directly adopts the preferred curvature of the clathrin coat and also that there is a dense packing of buds. Our model does not need to make these assumptions, and we feel that the observations of Saleem et al. can be equally well explained in the context of our modeling framework.

To this point, we have stated that the difference in energy requirement between the open and closed buds in the intermediate tension case is the likely explanation for the appearance of stalled pits in the absence of actin polymerization. An alternative explanation is that clathrin reorganization might be necessary for the clathrin coat to adopt the highly curved, post-snapthrough shape and the coat could be kinetically “trapped” in the open morphology. In order to form closed buds, clathrin triskelia form a meshwork consisting of hexagons and pentagons, similar to a soccer ball [54]. A flatter clathrin morphology has relatively more hexagons and so rearrangement of the clathrin lattice would be necessary to facilitate the incorporation of pentagons required for a highly curved morphology [12]. This rearrangement would require turnover of the clathrin triskelia as it would be extremely energetically costly to rearrange the lattice while attached to the membrane [9]. Continuous turnover of clathrin at endocytic sites has been observed by fluorescence recovery after photobleaching with a half-time of  $\approx 2$  seconds [37]. While relatively rapid on the timescale of CME, this might still be too slow to facilitate the snapthrough transition. Each clathrin triskelia transiently lost would decrease the effective size and spontaneous curvature of the coat, and the membrane would then equilibrate to a shape further from the snapthrough transition. This suggests that a potential role for actin polymer-

ization or BAR-domain proteins could be to maintain membrane curvature during the transition as the clathrin turns over and the lattice reorganizes.

One aspect of CME not explicitly addressed by this study is that the endocytic machinery includes curvature-generating proteins outside of the coat proteins and the actin machinery. In particular, recent modeling studies have demonstrated that cylindrical curvature induced by BAR-domain proteins can play an important role in reducing the force requirement for productive CME in yeast [23, 33]. However, CME is still productive in 50% of events even with complete knockout of the endocytic BAR-domain proteins in this organism [55], while actin assembly is absolutely required [21, 56]. Additionally, in mammalian cells a large percentage of CCPs were found to stall at high membrane tension when actin is inhibited [8] despite the fact that the BAR-domain proteins were presumably unaffected. These results suggest that while curvature generated by BAR-domain proteins may help to facilitate productive CME, force from actin assembly seems to be most important in challenging mechanical environments.

Though we have primarily focused on the impact of membrane tension on CME, our findings are general to any budding process. For example, it has been shown that membrane deformation by COPI coats is also inhibited by membrane tension [57]. Since the membranes of the endoplasmic reticulum and the Golgi are also under tension [58], one would expect that the shape evolution of buds from these organelles to also be determined by a balance of the coat spontaneous curvature, bending rigidity and membrane tension. Other membrane invaginations are also presumably governed by a similar set of physical parameters. For example, caveolae have been proposed to act as a membrane reservoir that buffers changes in membrane tension by disassembling upon an increase in membrane tension [50]. A similar framework to the one used in this study might provide some insight into the morphology and energetics of this process. Moving forward, more detailed measurements of both the membrane tension within cells as well as the spontaneous curvature of various membrane-bending proteins will be essential to verify and extend the results presented here.

## Acknowledgements

The authors would like to thank Matt Akamatsu and Charlotte Kaplan for critical reading of the manuscript. Charlotte Kaplan and Alba Diz-Muñoz performed membrane tension measurements referenced in the discussion. This research was supported by a National Defense Science and Engineering Graduate Fellowship to J.E.H, the National Institutes of Health Grant R01GM104979 to G.O. and the UC Berkeley Chancellor’s Postdoctoral Fellowship, and the Air Force Office of Scientific Research award number FA9550-15-1-0124 to P.R.

## References

1. Hochmuth, F., Shao, J.-Y., Dai, J. & Sheetz, M. P. Deformation and flow of membrane into tethers extracted from neuronal growth cones. *Biophysical journal* **70**, 358 (1996).
2. Diz-Muñoz, A., Fletcher, D. & Weiner, O. D. Use the force: membrane tension as an organizer of cell shape and motility. *Trends in Cell Biology* **23**, 47–53 (2013).
3. Houk, A. R. *et al.* Membrane tension maintains cell polarity by confining signals to the leading edge during neutrophil migration. *Cell* **148**, 175–188 (2012).
4. Dai, J., Ting-Beall, H. P. & Sheetz, M. P. The secretion-coupled endocytosis correlates with membrane tension changes in RBL 2H3 cells. *The Journal of general physiology* **110**, 1–10 (1997).
5. Gauthier, N. C., Fardin, M. A., Roca-Cusachs, P. & Sheetz, M. P. Temporary increase in plasma membrane tension coordinates the activation of exocytosis and contraction during cell spreading. *Proceedings of the National Academy of Sciences* **108**, 14467–14472 (2011).
6. Shi, Z. & Baumgart, T. Membrane tension and peripheral protein density mediate membrane shape transitions. *Nature communications* **6** (2015).
7. Stachowiak, J., Brodsky, F. & Miller, E. A cost-benefit analysis of the physical mechanisms of membrane curvature. *Nature Cell Biology* **15**, 1019–27 (2013).
8. Boulant, S., Kural, C., Zeeh, J.-C., Ubelmann, F. & Kirchhausen, T. Actin dynamics counteract membrane tension during clathrin-mediated endocytosis. *Nature Cell Biology* **13**, 1124–1131 (2011).
9. Saleem, M. *et al.* A balance between membrane elasticity and polymerization energy sets the shape of spherical clathrin coats. *Nature Communications* **6** (2015).
10. Doherty, G. J. & McMahon, H. T. Mechanisms of endocytosis. *Annual review of biochemistry* **78**, 857–902. ISSN: 0066-4154 (2009).
11. McMahon, H. T. & Boucrot, E. Molecular mechanism and physiological functions of clathrin-mediated endocytosis. *Nature reviews. Molecular Cell Biology* **12**, 517–533 (2011).
12. Kirchhausen, T., Owen, D. & Harrison, S. C. Molecular structure, function, and dynamics of clathrin-mediated membrane traffic. *Cold Spring Harbor perspectives in biology* **6**, a016725 (2014).
13. Liu, J., Sun, Y., Drubin, D. G. & Oster, G. F. The mechanochemistry of endocytosis. *PLoS Biology* **7**, e1000204 (2009).
14. Liu, J., Sun, Y., Oster, G. F. & Drubin, D. G. Mechanochemical crosstalk during endocytic vesicle formation. *Current opinion in cell biology* **22**, 36–43 (2010).

15. Dannhauser, P. & Ungewickell, E. Reconstitution of clathrin-coated bud and vesicle formation with minimal components. *Nature Cell Biology* **14**, 634–9 (2012).
16. Ford, M. *et al.* Curvature of clathrin-coated pits driven by epsin. *Nature* **419**, 361–366 (2002).
17. Stachowiak, J. *et al.* Membrane bending by protein-protein crowding. *Nature Cell Biology* **14**, 944–949 (2012).
18. Busch, D. J. *et al.* Intrinsically disordered proteins drive membrane curvature. *Nat Communications* **6**. <http://dx.doi.org/10.1038/ncomms8875> (July 2015).
19. Helfrich, W. Elastic properties of lipid bilayers: theory and possible experiments. *Zeitschrift für Naturforschung C* **28**, 693–703 (1973).
20. Lipowsky, R. Spontaneous tubulation of membranes and vesicles reveals membrane tension generated by spontaneous curvature. *Faraday discussions* **161**, 305–331 (2013).
21. Basu, R., Munteanu, E. L. & Chang, F. Role of turgor pressure in endocytosis in fission yeast. *Molecular Biology of the Cell* **25**, 679–872 (2013).
22. Miller, S. E. *et al.* CALM Regulates Clathrin-Coated Vesicle Size and Maturation by Directly Sensing and Driving Membrane Curvature. *Developmental Cell* **33**, 163–75 (2015).
23. Dmitrieff, S. & Nédélec, F. Membrane Mechanics of Endocytosis in Cells with Turgor. *PLOS Computational Biology*, 1–15 (2015).
24. Dai, J. & Sheetz, M. Membrane tether formation from blebbing cells. *Biophysical Journal* **77**, 3363–3370 (1999).
25. Yarar, D., Waterman-Storer, C. M. & Schmid, S. L. A dynamic actin cytoskeleton functions at multiple stages of clathrin-mediated endocytosis. *Molecular biology of the cell* **16**, 964–975 (2005).
26. Kukulski, W., Schorb, M., Kaksonen, M. & Briggs, J. a. G. Plasma membrane reshaping during endocytosis is revealed by time-resolved electron tomography. *Cell* **150**, 508–520 (2012).
27. Picco, A., Mund, M., Ries, J., Nédélec, F. & Kaksonen, M. Visualizing the functional architecture of the endocytic machinery. *eLife*. doi:10.7554/eLife.04535 (2015).
28. Grassart, A. *et al.* Actin and dynamin2 dynamics and interplay during clathrin-mediated endocytosis. *Journal of Cell Biology* **205**, 721–735 (2014).
29. Aguet, F., Antonescu, C. N., Mettlen, M., Schmid, S. L. & Danuser, G. Advances in analysis of low signal-to-noise images link dynamin and AP2 to the functions of an endocytic checkpoint. *Developmental Cell* **26**, 279–291. ISSN: 15345807 (2013).

30. Dai, J. & Sheetz, M. Mechanical properties of neuronal growth cone membranes studied by tether formation with laser optical tweezers. *Biophysical Journal* **68**, 988–96 (1995).
31. Dai, J., Sheetz, M., Wan, X. & Morris, C. Membrane tension in swelling and shrinking molluscan neurons. *The Journal of Neuroscience* **18**, 6681–92 (1998).
32. Liu, J., Kaksonen, M., Drubin, D. G. & Oster, G. Endocytic vesicle scission by lipid phase boundary forces. *Proceedings of the National Academy of Sciences of the United States of America* **103**, 10277–82. ISSN: 0027-8424 (2006).
33. Walani, N., Torres, J. & Agrawal, A. Endocytic proteins drive vesicle growth via instability in high membrane tension environment. *Proceedings of the National Academy of Sciences of the United States of America* **112**, E1423–E1432 (2015).
34. Carlsson, A. E. & Bayly, P. V. Force Generation by Endocytic Actin Patches in Budding Yeast. *Biophysical Journal* **106**, 1596–1606 (2012).
35. Zhang, T., Sknepnek, R., Bowick, M. & Schwarz, J. On the Modeling of Endocytosis in Yeast. *Biophysical Journal* **108**, 508–519. ISSN: 00063495 (2015).
36. Collins, A., Warrington, A., Taylor, K. a. & Svitkina, T. Structural organization of the actin cytoskeleton at sites of clathrin-mediated endocytosis. *Current biology : CB* **21**, 1167–75. ISSN: 1879-0445 (2011).
37. Avinoam, O., Schorb, M., Beese, C., Briggs, J. & Kaksonen, M. Endocytic sites mature by continuous bending and remodeling of the clathrin coat. *Science* **348**, 1369–1372 (2015).
38. Taylor, M. J., Perrais, D. & Merrifield, C. J. A high precision survey of the molecular dynamics of mammalian clathrin-mediated endocytosis. *PLoS Biol* **9**, e1000604 (2011).
39. Rawicz, W., Olbrich, K. C., McIntosh, T., Needham, D & Evans, E. Effect of chain length and unsaturation on elasticity of lipid bilayers. *Biophysical journal* **79**, 328–339. ISSN: 00063495 (2000).
40. Rangamani, P., Mandadapu, K. & Oster, G. Protein-induced membrane curvature alters local membrane tension. *Biophysical Journal* **107**, 751–762 (2014).
41. Bassereau, P., Sorre, B. & Lévy, A. Bending lipid membranes: Experiments after W. Helfrich’s model. *Advances in colloid and interface science* **208**, 47–57 (2014).
42. Agrawal, A. & Steigmann, D. Modeling protein-mediated morphology in biomembranes. *Biomechanics and modeling in mechanobiology* **8**, 371–379 (2009).
43. Steigmann, D., Baesu, E., Rudd, R. E., Belak, J. & McElfresh, M. On the variational theory of cell-membrane equilibria. *Interfaces and Free Boundaries* **5**, 357–366 (2003).

44. Steigmann, D. J. Fluid films with curvature elasticity. *Archive for Rational Mechanics* **150**, 127–52 (1999).
45. Sens, P. & Plastino, J. Membrane tension and cytoskeleton organization in cell motility. *Journal of Physics: Condensed Matter* **27**, 273103 (2015).
46. Jin, A. J., Prasad, K., Smith, P. D., Lafer, E. M. & Nossal, R. Measuring the elasticity of clathrin-coated vesicles via atomic force microscopy. *Biophysical journal* **90**, 3333–3344 (2006).
47. Zimmerberg, J. & Kozlov, M. M. How proteins produce cellular membrane curvature. *Nature Reviews: Molecular Cell Biology* **7**, 9–19 (2006).
48. Bieling, P. *et al.* Force Feedback Controls Motor Activity and Mechanical Properties of Self-Assembling Branched Actin Networks. *Cell* **164**, 115–127. ISSN: 0092-8674 (2016).
49. Sirotkin, V., Berro, J., Macmillan, K., Zhao, L. & Pollard, T. D. Quantitative Analysis of the Mechanism of Endocytic Actin Patch Assembly and Disassembly in Fission Yeast. *Molecular biology of the cell*. ISSN: 1939-4586. doi:10.1091/mbc.E10 (2010).
50. Sinha, B. *et al.* Cells respond to mechanical stress by rapid disassembly of caveolae. *Cell* **144**, 402–413 (2011).
51. Honigsmann, A. *et al.* A lipid bound actin meshwork organizes liquid phase separation in model membranes. *Elife* **3**, e01671 (2014).
52. Trimble, W. S. & Grinstein, S. Barriers to the free diffusion of proteins and lipids in the plasma membrane. *The Journal of Cell Biology* **208**, 259–271 (2015).
53. Fujiwara, T. K. *et al.* Confined diffusion of transmembrane proteins and lipids induced by the same actin meshwork lining the plasma membrane. *Molecular biology of the cell*, mbc–E15 (2016).
54. Kirchhausen, T. Clathrin. *Annual review of biochemistry* **69**, 699–727 (2000).
55. Kishimoto, T. *et al.* Determinants of endocytic membrane geometry, stability, and scission. *Proceedings of the National Academy of Sciences* **108**, E979–E988 (2011).
56. Kaksonen, M., Sun, Y. & Drubin, D. G. A pathway for association of receptors, adaptors, and actin during endocytic internalization. *Cell* **115**, 475–487 (2003).
57. Manneville, J.-B. *et al.* COPI coat assembly occurs on liquid-disordered domains and the associated membrane deformations are limited by membrane tension. *Proceedings of the National Academy of Sciences* **105**, 16946–16951 (2008).
58. Upadhyaya, A. & Sheetz, M. P. Tension in tubulovesicular networks of Golgi and endoplasmic reticulum membranes. *Biophysical journal* **86**, 2923–2928 (2004).



59. Doyon, J. *et al.* Rapid and efficient clathrin-mediated endocytosis revealed in genome-edited mammalian cells. *Nature Cell Biology* **13**, 331–337 (2011).
60. Rangamani, P., Agrawal, A., Mandadapu, K. K., Oster, G. & Steigmann, D. J. Interaction between surface shape and intra-surface viscous flow on lipid membranes. *Biomechanics and modeling in mechanobiology* **12**, 833–45 (2013).
61. Derényi, I., Jülicher, F. & Prost, J. Formation and interaction of membrane tubes. *Physical review letters* **88**, 238101 (2002).

# Supplemental material for ‘Membrane tension is a key determinant of bud morphology in clathrin-mediated endocytosis’

Julian E. Hassinger<sup>1</sup>, George Oster<sup>2</sup>, David G. Drubin<sup>2</sup>, and <sup>3</sup>Padmini Rangamani

<sup>1</sup>Biophysics Graduate Group, University of California, Berkeley

<sup>2</sup>Department of Molecular and Cell Biology, University of California, Berkeley

<sup>3</sup>Department of Mechanical and Aerospace Engineering, University of California, San Diego

## Contents

<b>1</b>	<b>Model description</b>	<b>2</b>
1.1	Assumptions . . . . .	2
1.2	Equilibrium equations . . . . .	2
1.2.1	Helfrich energy elastic model . . . . .	3
1.3	Equations of motion in axisymmetric coordinates . . . . .	4
1.3.1	Definitions . . . . .	4
1.3.2	Equilibrium equations . . . . .	5
1.3.3	Boundary conditions . . . . .	5
1.3.4	Dimensionless variables . . . . .	6
1.4	Area dependence . . . . .	6
1.4.1	Arc-length to area dependence . . . . .	6
1.4.2	Dimensionless variables . . . . .	7
<b>2</b>	<b>Simulation Methods</b>	<b>8</b>
<b>3</b>	<b>Computation of the energy to deform the membrane</b>	<b>9</b>
<b>4</b>	<b>Tables</b>	<b>11</b>
<b>5</b>	<b>Supplementary Figures</b>	<b>13</b>

# 1 Model description

## 1.1 Assumptions

1. The lipid bilayer is modeled as a two-dimensional differentiable manifold endowed with mechanical properties. Helfrich proposed a model that treats the manifold as a thin elastic shell whose bending behavior is captured by an energy density functional that depends only on the manifold's local curvatures [19]. This model and its variants are valid for radii of curvatures much larger than the membrane thickness. We assume that the Helfrich energy is sufficient to describe the membrane during clathrin-mediated endocytosis.
2. The membrane is assumed to be at mechanical equilibrium at all times. Because clathrin-mediated endocytosis occurs over a timescale of tens of seconds [8, 28, 29, 38, 59], this assumption is valid [13, 23]. We do not include explicit time dependence arising from the viscosity of the bilayer or the surrounding fluid or due to diffusion. This is a focus of future work.
3. The lipid bilayer is assumed to be incompressible, based on a large stretch modulus [39]. This constraint is introduced using a Lagrange multiplier  $\gamma$  (see Table 1 for notation).
4. Protein adsorption on the membrane (*i.e.* the clathrin coat) is represented using spontaneous curvature ( $C$ ). Since we are modeling the membrane as a single manifold, the notion of intrinsic curvature due to different lipids or proteins interacting with each leaflet is represented by this term [19, 40, 42].
5. For ease of computation, we assume that endocytic pit is rotationally symmetric. This allows us to obtain solutions capturing the whole budding process with a relatively simple parameterization of the surface.

## 1.2 Equilibrium equations

Here we present a concise derivation of the equilibrium equations for biological membranes. Detailed derivations are presented in [42, 44, 60].

The local force balance, based on the conservation of linear momentum, and in the absence of inertia is

$$\mathbf{div} \boldsymbol{\sigma} + p\mathbf{n} = \mathbf{f}. \quad (\text{S1})$$

Here,  $\mathbf{div}$  denotes the surface divergence,  $\boldsymbol{\sigma}$  are the stress vectors,  $p$  is the pressure difference across the membrane,  $\mathbf{n}$  is the surface normal, and  $\mathbf{f}$  is the externally applied force. The surface stresses can be expressed as

$$\boldsymbol{\sigma}^\alpha = \mathbf{T}^\alpha + S^\alpha \mathbf{n}, \quad (\text{S2})$$

and the surface divergence is expressed as

$$\mathbf{div} \boldsymbol{\sigma} = \boldsymbol{\sigma}_{;\alpha}^\alpha = (\sqrt{a})^{-1}(\sqrt{a}\boldsymbol{\sigma}^\alpha)_{,\alpha}. \quad (\text{S3})$$

$(\cdot)_{;\alpha}$  denotes the covariant derivative. It should be noted that  $\mathbf{T}^\alpha$  and  $S^\alpha$  need to be constitutively determined. In this case, if  $F(H, K; x^\alpha)$  is the elastic energy density per unit mass of the surface [44, 60], then  $S^\alpha$  and the individual components of the  $\mathbf{T}^\alpha$  are given by

$$\mathbf{T}^\alpha = T^{\beta\alpha} \mathbf{a}_\beta \quad \text{with} \quad T^{\beta\alpha} = \sigma^{\beta\alpha} + b_\mu^\beta M^{\mu\alpha}, \quad \text{and} \quad S^\alpha = -M_{;\beta}^{\alpha\beta}, \quad (\text{S4})$$

where

$$\sigma^{\beta\alpha} = \rho \left( \frac{\partial F}{\partial a_{\alpha\beta}} + \frac{\partial F}{\partial a_{\beta\alpha}} \right) \quad \text{and} \quad M^{\beta\alpha} = \frac{1}{2} \rho \left( \frac{\partial F}{\partial b_{\alpha\beta}} + \frac{\partial F}{\partial b_{\beta\alpha}} \right), \quad (\text{S5})$$

see [44] for a full derivation. For an elastic membrane that responds to out-of-plane bending and is area incompressible, the general form for the free energy density per unit mass can be rewritten as

$$F(\rho, H, K; x^\alpha) = \bar{F}(H, K; x^\alpha) - \gamma(x^\alpha, t)/\rho, \quad (\text{S6})$$

where  $\gamma(x^\alpha, t)$  is a Lagrange multiplier required to implement the constraint  $\rho(x^\alpha, t)$  is constant or the local area dilation  $J = 1$ ,  $H$  and  $K$  are the mean and Gaussian curvatures respectively. Substituting  $W = \rho \bar{F}$  and invoking the definitions of the mean and Gaussian curvatures,  $H = \frac{1}{2} a^{\alpha\beta} b_{\alpha\beta}$  and  $K = \frac{1}{2} \varepsilon^{\alpha\beta} \varepsilon^{\lambda\mu} b_{\alpha\lambda} b_{\beta\mu}$ , in terms of the induced metric and curvature tensors  $a^{\alpha\beta} = (a_{\alpha\beta})^{-1}$  and  $b^{\alpha\beta} = a^{\alpha\lambda} a^{\beta\mu} b_{\lambda\mu}$ , respectively, Eq. (S6) can be rewritten as

$$\begin{aligned} \sigma^{\alpha\beta} &= (\lambda + W) a^{\alpha\beta} - (2HW_H + 2KW_K) a^{\alpha\beta} + W_H \tilde{b}^{\alpha\beta}, \\ M^{\alpha\beta} &= \frac{1}{2} W_H a^{\alpha\beta} + W_K \tilde{b}^{\alpha\beta}, \end{aligned} \quad (\text{S7})$$

where

$$\lambda = -(\gamma + W). \quad (\text{S8})$$

Using Eqs. (S7), (S4) and (S2), the equations of motion Eq. (S1) can then be reduced to

$$p + \mathbf{f} \cdot \mathbf{n} = \Delta \left( \frac{1}{2} W_H \right) + (W_K)_{;\alpha\beta} \tilde{b}^{\alpha\beta} + W_H (2H^2 - K) + 2H(KW_K - W) - 2\lambda H, \quad (\text{S9})$$

and

$$N_{;\alpha}^{\beta\alpha} - S^{\alpha} b_{\alpha}^{\beta} = -(\gamma_{,\alpha} + W_K K_{,\alpha} + W_H H_{,\alpha}) a^{\beta\alpha} = (\partial W / \partial x_{|\text{exp}}^{\alpha} + \lambda_{,\alpha}) a^{\beta\alpha} = 0, \quad (\text{S10})$$

Here  $\Delta(\cdot) = (\cdot)_{;\alpha\beta} a^{\alpha\beta}$  is the surface Laplacian and  $(\cdot)_{|\text{exp}}$  represents the explicit derivative with respect to  $\theta^\alpha$ .

### 1.2.1 Helfrich energy elastic model

For a lipid-bilayer membrane, the local elastic energy takes the Helfrich energy form

$$W = k(H - C(\theta^\alpha))^2 + \bar{k}K \quad (\text{S11})$$

where  $C(\theta^\alpha)$  is the spontaneous curvature that can depend on the coordinates. This energy function differs from the standard Helfrich energy by a factor of 2, with the net effect being that our value for the bending modulus,  $k$ , is twice that of the standard bending modulus typically encountered in the literature [19]. The Gaussian modulus is assumed to be uniform, and the membrane is planar at the boundary of the simulated domain.

The equations of motion (S9) and (S10) for an elastic membrane reduce to

$$k\Delta(H - C) + 2k(H - C)(2H^2 - K) - 2kH(H - C)^2 = p + 2\lambda H + \mathbf{f} \cdot \mathbf{n}, \quad (\text{S12})$$

$$\lambda_{,\gamma} = -\frac{\partial W}{\partial x^\gamma} = 2k(H - C)\frac{\partial C}{\partial x^\gamma} - \mathbf{f} \cdot \mathbf{a}_\gamma. \quad (\text{S13})$$

In the absence of externally applied force  $\mathbf{f}$ , we recover the equations of motion for a heterogeneous membrane [40, 42].

$$\lambda_{,\gamma} = -\frac{\partial W}{\partial x^\gamma}|_{\text{exp}} = 2k(H - C)\frac{\partial C}{\partial x^\gamma}. \quad (\text{S14})$$

$$k[\Delta(H - C) + 2(H - C)(H^2 + HC - K)] - 2\lambda H = p. \quad (\text{S15})$$

$\lambda$  can be interpreted as the tension in a flat membrane [44, 60]. Furthermore, in the special case of zero spontaneous curvature and non-zero mean curvature,  $\lambda = \text{constant}$  everywhere, see Eq. (S13). This constant value of  $\lambda$  must be provided as an input parameter to solve the system of equations [44], and is widely interpreted to be surface tension in the literature [61]. A detailed interpretation of  $\lambda$  is given in [40].

### 1.3 Equations of motion in axisymmetric coordinates

#### 1.3.1 Definitions

We define a surface of revolution (see Figure S1)

$$\mathbf{r}(s, \theta) = r(s)\mathbf{e}_r(\theta) + z(s)\mathbf{k} \quad (\text{S16})$$

where  $s$  is the arc-length along the curve,  $r(s)$  is the radius from axis of revolution,  $z(s)$  is the elevation from a base plane and  $(\mathbf{e}_r, \mathbf{e}_\theta, \mathbf{k})$  form the coordinate basis. Since  $(r')^2 + (z')^2 = 1$ , we can define an angle  $\psi$  such that

$$\mathbf{a}_s = \cos \psi \mathbf{e}_r + \sin \psi \mathbf{k}, \quad \mathbf{n} = -\sin \psi \mathbf{e}_r + \cos \psi \mathbf{k} \quad (\text{S17})$$

are the unit tangent and normal vectors, respectively, and

$$r'(s) = \cos \psi, \quad z'(s) = \sin \psi \quad (\text{S18})$$

parametrize the surface. The tangential ( $\kappa_\nu$ ) and transverse ( $\kappa_t$ ) curvatures are given by

$$\kappa_\nu = \psi, \quad \kappa_t = r^{-1} \sin \psi \quad (\text{S19})$$

and the mean ( $H$ ) and Gaussian ( $K$ ) curvatures

$$H = \frac{1}{2}(\kappa_\nu + \kappa_t) \quad (\text{S20})$$

$$K = \kappa_\nu \kappa_t = H^2 - (H - r^{-1} \sin \psi)^2. \quad (\text{S21})$$

Rearranging Eq. (S20) with Eq. (S19) yields the differential equation for  $\psi$ ,

$$r\psi'(s) = 2rH - \sin \psi. \quad (\text{S22})$$

### 1.3.2 Equilibrium equations

Let  $L$  be given by

$$L = \frac{1}{2k} r (W_H)' = r (H - C)', \quad (\text{S23})$$

allowing us to obtain a first-order differential equation for the mean curvature,

$$H'(s) = r^{-1} L + C'(s). \quad (\text{S24})$$

Using Eq. (S23) in Eq. (S12) we obtain

$$k\Delta(H - C) = k [(H - C)']' = kr^{-1} [L]' = kr^{-1} L'. \quad (\text{S25})$$

Inserting Eq. (S25) into Eq. (S12) and rearranging we obtain a first-order differential equation for  $L$ ,

$$\begin{aligned} kr^{-1} L' + 2k(H - C)(2H^2 - K) - 2kH(H - C)^2 &= p + 2\lambda H + \mathbf{f} \cdot \mathbf{n} \\ kr^{-1} L' &= p + \mathbf{f} \cdot \mathbf{n} + 2H \left[ k(H - C)^2 + \lambda \right] - 2k(H - C) \left[ H^2 + (H - r^{-1} \sin \psi)^2 \right] \\ r^{-1} L'(s) &= \frac{p}{k} + \frac{\mathbf{f} \cdot \mathbf{n}}{k} + 2H \left[ (H - C)^2 + \frac{\lambda}{k} \right] - 2(H - C) \left[ H^2 + (H - r^{-1} \sin \psi)^2 \right]. \end{aligned} \quad (\text{S26})$$

Finally, Eq. (S13) becomes

$$\lambda'(s) = 2k(H - C)C'(s) - \mathbf{f} \cdot \mathbf{a}_s. \quad (\text{S27})$$

The system of equations to be solved to obtain the shapes of the membrane are Eqs. (S18), (S22), (S24), (S26), and (S27).

### 1.3.3 Boundary conditions

In order to solve this system of equations, we need to provide six boundary conditions. We consider an axisymmetric circular patch of membrane (see Figure S1). At the center of the patch,  $s = 0^+$ , we require: 1) the distance from the axis of symmetry be 0, 2)  $\psi = 0$  to ensure continuous differentiability of the surface, and 3)  $L = 0$  due to reflection symmetry. At the boundary of the patch,  $s = S$ , we require 1) that the membrane not lift off and therefore  $Z = 0$ , 2)  $\psi = 0$  to ensure continuous differentiability with the flat surrounding membrane, and 3)  $\lambda$  is prescribed. These conditions can be summarized as

$$R(0^+) = 0, \quad L(0^+) = 0, \quad \psi(0^+) = 0, \quad (\text{S28a})$$

$$Z(S) = 0, \quad \psi(S) = 0, \quad \lambda(S) = \lambda_0. \quad (\text{S28b})$$

In cases relating to the actin-mediated pulling (Figure 8), we prescribe the displacement of the tip, and calculate the force needed to maintain the prescribed displacement. We implement this additional boundary condition as

$$Z(0^+) = Z_p. \quad (\text{S29})$$

Similarly, for actin-mediated pinching (Figure S11), we prescribe the mean curvature at the bud tip and calculate the force required to maintain this curvature. This boundary condition is implemented as

$$H(0^+) = H_p. \quad (\text{S30})$$

### 1.3.4 Dimensionless variables

In order to perform the numerical computations, we non-dimensionalized the system by introducing two positive constants,  $R_0$  and  $k_0$ , and defining the following dimensionless variables.

$$\begin{aligned} t &\equiv s/R_0, & x &\equiv r/R_0, & y &\equiv z/R_0, & h &\equiv HR_0, & c &\equiv CR_0, \\ l &\equiv LR_0, & \tilde{\lambda} &\equiv \lambda R_0^2/k_0, & \tilde{p} &\equiv pR_0^3/k_0, & \tilde{\mathbf{f}} &\equiv \mathbf{f}R_0^3/k_0, & \tilde{k} &\equiv k/k_0. \end{aligned} \quad (\text{S31})$$

In terms of Eq. (S31), the system of equations, Eqs. (S18), (S22), (S24), (S26), and (S27), become

$$\dot{x} = \cos \psi, \quad \dot{y} = \sin \psi, \quad x\dot{\psi} = 2xh - \sin \psi, \quad \dot{h} = x^{-1}l + \dot{c} \quad (\text{S32a})$$

$$x^{-1}\dot{l} = \frac{\tilde{p}}{\tilde{k}} + \frac{\tilde{\mathbf{f}} \cdot \mathbf{n}}{\tilde{k}} + 2h \left[ (h-c)^2 + \frac{\tilde{\lambda}}{\tilde{k}} \right] - 2(h-c) \left[ h^2 + (h-x^{-1}\sin \psi)^2 \right] \quad (\text{S32b})$$

$$\dot{\tilde{\lambda}} = 2\tilde{k}(h-c)\dot{c} - \tilde{\mathbf{f}} \cdot \mathbf{a}_s \quad (\text{S32c})$$

the boundary conditions, Eq. (S28) become

$$x(0^+) = 0, \quad l(0^+) = 0, \quad \psi(0^+) = 0 \quad (\text{S33a})$$

$$\psi(T) = 0, \quad y(T) = 0, \quad \tilde{\lambda}(T) = \tilde{\lambda}_0, \quad (\text{S33b})$$

where  $T = S/R_0$  is the total dimensionless arc-length. The boundary conditions imposed to solve for unknown applied force, Eqs. (S29) and (S30), become

$$y(0^+) = y_p, \quad h(0^+) = h_p. \quad (\text{S34})$$

## 1.4 Area dependence

### 1.4.1 Arc-length to area dependence

In axisymmetry there is a one-to-one correspondence between arc-length and area, which allows us to express the system of equations as a function of area instead of arc-length. This is because

$$a(s) = 2\pi \int_0^s r(t)dt \quad \implies \quad \frac{da}{ds} = 2\pi r. \quad (\text{S35})$$

This method has the advantage of prescribing the total membrane area rather than the arc length as the simulation domain. Using Eq. (S35), we convert Eqs. (S18), (S22), (S24), (S26), and (S27) into

$$2\pi r r'(a) = \cos \psi, \quad 2\pi r z'(a) = \sin \psi, \quad 2\pi r^2 \psi'(a) = 2rH - \sin \psi, \quad (\text{S36a})$$

$$2\pi r^2 H'(a) = L + 2\pi r^2 C'(a) \quad (\text{S36b})$$

$$2\pi L'(a) = \frac{p}{k} + \frac{\mathbf{f} \cdot \mathbf{n}}{k} + 2H \left[ (H - C)^2 + \frac{\lambda}{k} \right] - 2(H - C) \left[ H^2 + (H - r^{-1} \sin \psi)^2 \right] \quad (\text{S36c})$$

$$2\pi r \lambda'(a) = 4\pi r k (H - C) C'(a) - \mathbf{f} \cdot \mathbf{a}_s, \quad (\text{S36d})$$

The boundary conditions, Eqs. (S28) and (S29) are remain unchanged except for the limits at which they are applied.

$$R(0^+) = 0, \quad L(0^+) = 0, \quad \psi(0^+) = 0, \quad (\text{S37a})$$

$$\psi(A) = 0, \quad Z(A) = 0, \quad \lambda(A) = \lambda_0, \quad (\text{S37b})$$

where  $A = 2\pi \int_0^S r(t)dt$  is the total area of the membrane patch. The displacement and mean curvature conditions are

$$Z(0^+) = Z_p, \quad H(0^+) = H_p. \quad (\text{S38})$$

### 1.4.2 Dimensionless variables

For Figures 2, 3, 7 and 8, we used non-dimensional area dependent equations. Using the two positive constants,  $R_0$  and  $k_0$ , we can define

$$\begin{aligned} \alpha &\equiv \frac{a}{2\pi R_0^2}, & x &\equiv r/R_0, & y &\equiv z/R_0, & h &\equiv HR_0, & c &\equiv CR_0, \\ l &\equiv LR_0, & \tilde{\lambda} &\equiv \lambda R_0^2/k_0, & \tilde{p} &\equiv pR_0^3/k_0, & \tilde{\mathbf{f}} &\equiv \mathbf{f}R_0^3/k_0, & \tilde{k} &\equiv k/k_0. \end{aligned} \quad (\text{S39})$$

In terms of Eq. (S39), the system of equations, Eq. (S36), become

$$x\dot{x} = \cos \psi, \quad x\dot{y} = \sin \psi, \quad x^2\dot{\psi} = 2xh - \sin \psi, \quad x^2\dot{h} = l + x^2\dot{c} \quad (\text{S40a})$$

$$\dot{l} = \frac{\tilde{p}}{\tilde{k}} + \frac{\tilde{\mathbf{f}} \cdot \mathbf{n}}{\tilde{k}} + 2h \left[ (h - c)^2 + \frac{\tilde{\lambda}}{\tilde{k}} \right] - 2(h - c) \left[ h^2 + (h - x^{-1} \sin \psi)^2 \right] \quad (\text{S40b})$$

$$\dot{\tilde{\lambda}} = 2\tilde{k}(h - c)\dot{c} - x^{-1}\tilde{\mathbf{f}} \cdot \mathbf{a}_s, \quad (\text{S40c})$$

and the boundary conditions, Eq. (S37) and Eq. (S38), become



$$x(0^+) = 0, \quad l(0^+) = 0, \quad \psi(0^+) = 0 \quad (\text{S41a})$$

$$y(\alpha_{max}) = 0, \quad \psi(\alpha_{max}) = 0, \quad \tilde{\lambda}(\alpha_{max}) = \tilde{\lambda}_0, \quad (\text{S41b})$$

$$y(0^+) = y_p \quad h(0^+) = h_p. \quad (\text{S41c})$$

where  $\alpha_{max} = \frac{A}{2\pi R_0^2}$  is the total dimensionless membrane area.

## 2 Simulation Methods

Computations were performed using MATLAB<sup>®</sup> (Mathworks, Natick, MA) using the routine ‘bvp4c’, a boundary value problem solver. All MATLAB<sup>®</sup> code used to perform the simulations can be found online as Supplemental files.

- The membrane patch is initialized to be a flat disk with a radius of  $R = 400$  nm.
  - The exception to this was for the simulations involving the creation of the phase diagram, Figure 5. In this case, the initial radius of the disk was set such that the arc-length of the domain was twice that needed for a bud of radius  $R = 1/C_0$ , where  $C_0$  is the spontaneous curvature of the coat.
- The mesh points on the domain were chosen such that they were (initially) equally spaced along the arc-length with a spacing of 0.5 nm. To obtain convergence, the solver was allowed to increase the number of mesh points by up to a factor of 100, with the final solution evaluated on the original mesh.
- Subsequently, the area (or arc-length) of the coat (with fixed spontaneous curvature) or the spontaneous curvature of the coat (with fixed coat area) were progressively increased, with each solution in this sequence used in the solver as the initial guess for the subsequent computation.
- To ensure sharp but smooth transitions at the boundaries of the coat and regions of applied force, these regions were specified using a hyperbolic tangent function (Figure S2).
- Simulations using the area-dependent equations (S40): Figures 2, 3, 7, 8, S3, and S5
  - This was the preferred method for solving the ODEs as the area of the membrane domain is kept constant throughout the entire simulation, meaning that the boundaries of the domain stayed relatively more constant than in the arc-length parametrization.
  - Despite this preference, we show in Figure S4 that the area of the membrane patch makes essentially no difference on the observed shapes of the membrane as long as the domain is sufficiently large, ensuring that either surface parametrization is valid and the solutions directly comparable.
  - Additionally, this parametrization is much more convenient in terms of directly specifying the coat area as well as the area of applied force. The applied force case is especially important as the applied force is really a force per unit area, or effective pressure (see Eq. (S12)), and the total magnitude of the force is obtained by integrating the force per unit area over the applied area.
- Simulations using the arc-length-dependent equations (S32): Figures 4 and 5

- Arc-length dependence was convenient for “coat-growing” simulations in the case of intermediate membrane tension as this formulation allowed for the instability to be smoothly traversed by simply increasing the arc-length coverage by the coat.
- This is because it is possible for the arc-length covered by the coat to increase while the area coverage of the coat simultaneously decreases if the membrane becomes much more highly curved in the coated region.
- This is exactly what happens for the so-called *unstable solutions* in Figure 4. These solutions cannot be accessed by the solver simply by adjusting the area of the coat; the next solution will always fall on one of the two *stable solution* branches. However, these unstable solutions are readily accessible simply by increasing the arc-length coverage of the coat, conveniently tracing out the entire solution space.
- Simulations with an applied force: Figures 8, S10, and S11
  - Rather than prescribing the force to obtain a displacement, we took advantage of the ability of the ‘bvp4c’ solver to calculate values of unknown parameters given an initial guess and an additional boundary condition.
  - For pulling forces (Figures 8 and S10), this was achieved by specifying the z-position of the tip of the bud Eq. (S38). For simplicity, the force was applied uniformly across the coat.
  - For squeezing forces (Figure S11), this was achieved by specifying the mean curvature at the tip of the bud Eq. (S38). For simplicity, the applied force was applied on a band of the membrane immediately bordering the coat.

### 3 Computation of the energy to deform the membrane

- The energy necessary to deform the membrane can be expressed as the sum of the work done against the bending rigidity, membrane tension, and pressure:

$$E_{\text{tot}} = E_{\text{bending}} + E_{\text{tension}} + E_{\text{pressure}} \quad (\text{S42})$$

- The bending energy is calculated by integrating the bending rigidity,  $k$ , times the square of the difference between the local mean curvature,  $H$ , and the local spontaneous curvature,  $C$ , over the area of the domain:

$$E_{\text{bending}} = \int_0^A k (H - C)^2 da \quad (\text{S43})$$

- For comparison, this is equivalent to integrating Eq. (S11) over the area of the domain.
- The work done against membrane tension is calculated by multiplying the edge membrane tension,  $\lambda_0$ , by the difference between the total and projected area of the domain:

$$E_{\text{tension}} = \lambda_0 (A_{\text{tot}} - A_{\text{proj}}) \quad (\text{S44})$$

- $(A_{\text{tot}} - A_{\text{proj}})$  represents the amount of area that must be pulled in from the surrounding membrane to accommodate the deformation of the membrane patch. Multiplication by the edge membrane tension (the value of the membrane tension in the surrounding membrane) gives the energy of the deformation.

- The projected area is simply the area of the disk obtained when the membrane deformation is projected onto the plane  $Z = 0$  nm. This quantity is easily calculated as  $A_{\text{proj}} = \pi R_{\text{bound}}^2$ , where  $R_{\text{bound}}$  is the radial distance to the boundary.
- In the case of arc-length dependence,  $A_{\text{tot}} = 2\pi \int_0^S r(t)dt$ , where  $S$  is the total arc-length. In the case of area dependence  $A_{\text{tot}}$  is simply the set value of the area of the domain.
- The work done against pressure is calculated by multiplying the transmembrane pressure,  $p$ , by the volume enclosed by the deformed membrane and the plane  $Z = 0$  nm,  $V_{\text{encl}}$ :

$$E_{\text{pressure}} = pV_{\text{encl}} \tag{S45}$$

- The enclosed volume is calculated as  $V_{\text{encl}} = \pi \int_{Z(a=0)}^{Z(a=A)} R(a)^2 dZ(a)$ .

## 4 Tables

Table 1: Notation used in the model

Notation	Description	Units
$W$	Local energy per unit area	pN/nm
$H$	Mean curvature of the membrane	nm <sup>-1</sup>
$K$	Gaussian curvature of the membrane	nm <sup>-2</sup>
$C$	Prescribed spontaneous curvature	nm <sup>-1</sup>
$\theta^\alpha$	Parameters describing the surface, $\alpha \in \{1, 2\}$	
$A_{\text{coat}}$	Area covered by the coat	nm <sup>2</sup>
$\mathbf{r}$	Position vector	
$\mathbf{n}$	Normal to the membrane surface	unit vector
$\mathbf{a}_\alpha$	Basis vectors describing the tangent plane, $\alpha \in \{1, 2\}$	
$\gamma$	Lagrange multiplier for the incompressibility constraint	pN/nm
$\lambda$	Membrane tension, $-(W + \gamma)$	pN/nm
$p$	Pressure difference across the membrane	pN/nm <sup>2</sup>
$\mathbf{f}$	Applied force per unit area	pN/nm <sup>2</sup>
$k$	Bending modulus	pN·nm
$\bar{k}$	Gaussian modulus	pN·nm
$s$	Arc-length	nm
$S$	Total arc-length of the membrane patch	nm
$\theta$	Azimuthal angle	
$r$	Radial distance	nm
$z$	Elevation from base plane	nm
$\mathbf{e}_r$	Radial basis vector	unit vector
$\mathbf{e}_\theta$	Azimuthal basis vector	unit vector
$\mathbf{k}$	Altitudinal basis vector	unit vector
$\mathbf{a}_s$	Tangent to the membrane surface in the radial direction	unit vector
$\psi$	Angle between $\mathbf{e}_r$ and $\mathbf{a}_s$	

Table 2: Notation used in the model (continued)

Notation	Description	Units
$\kappa_\nu$	Tangential curvature	$\text{nm}^{-1}$
$\kappa_t$	Transverse curvature	$\text{nm}^{-1}$
$L$	Shape equation variable	$\text{nm}^{-1}$
$Z_p$	Prescribed displacement at the pole	$\text{nm}$
$H_p$	Prescribed mean curvature at the pole	$\text{nm}^{-1}$
$t$	Dimensionless arc-length	
$x$	Dimensionless radial distance	
$y$	Dimensionless height	
$h$	Dimensionless mean curvature	
$c$	Dimensionless spontaneous curvature	
$l$	Dimensionless $L$	
$\tilde{\lambda}$	Dimensionless membrane tension	
$\tilde{p}$	Dimensionless transmembrane pressure	
$\tilde{\mathbf{f}}$	Dimensionless force per unit area	
$\tilde{k}$	Dimensionless bending rigidity	
$T$	Total dimensionless arc-length	
$y_p$	Dimensionless prescribed pole displacement	
$H_p$	Dimensionless prescribed pole mean curvature	
$a$	Membrane area	$\text{nm}^2$
$A$	Total area of membrane patch	$\text{nm}^2$
$\alpha$	Dimensionless membrane area	
$\alpha_{max}$	Total dimensionless area	

Table 3: Parameters used in the model

Parameter	Significance	Value	Reference
$\lambda_0$	Membrane tension range	$10^{-4} - 1 \text{ pN/nm}$	[7, 31, 45]
$k$	Bending rigidity of bare membrane	$320 \text{ pN} \cdot \text{nm}$	[7]
$C_0$	Preferred curvature of coat	$1/50 \text{ nm}^{-1}$	[7, 22]
$R_0$	Non-dimensionalization length	$20 \text{ nm}$	

## 5 Supplementary Figures

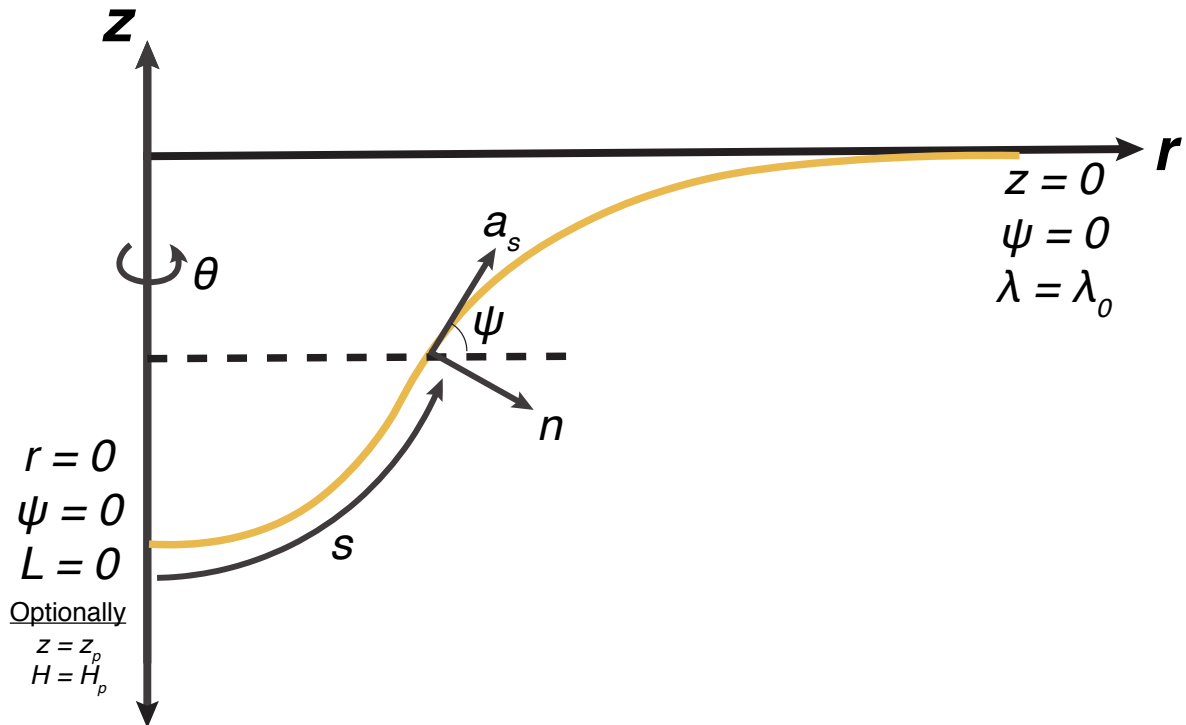


Figure S1: Schematic of the axisymmetric geometry adopted for the simulations as described in Section 1.3. The boundary conditions at the tip of the bud and the boundary of the patch were implemented as indicated. The optional boundary conditions (S29) and (S30) were used to obtain the value of applied force in actin-mediated pulling (Figure 8) and pinching (Figure S11) simulations, respectively (see Section 1.3.3).

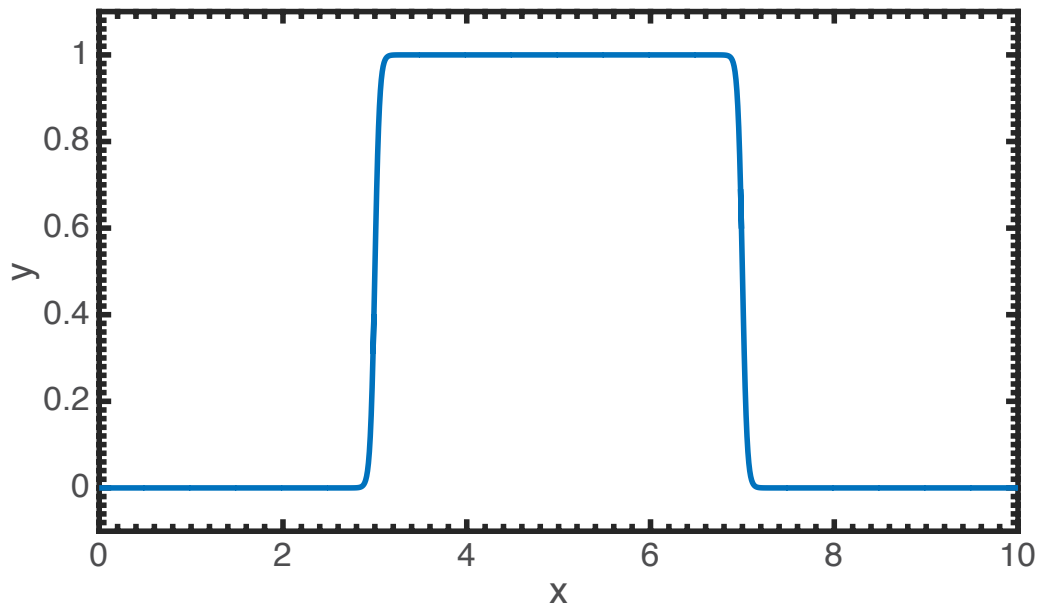


Figure S2: A hyperbolic tangent functional form was used to implement heterogeneous membrane properties. As an example,  $y = \frac{1}{2} [\tanh(\gamma(x - 3)) - \tanh(\gamma(x - 7))]$  is plotted with  $\gamma = 20$ . The sharp transitions were ideal for specifying the boundaries of the coated region or regions of applied force, and the smoothness of the tanh function allowed for straightforward implementation into the numerical scheme.

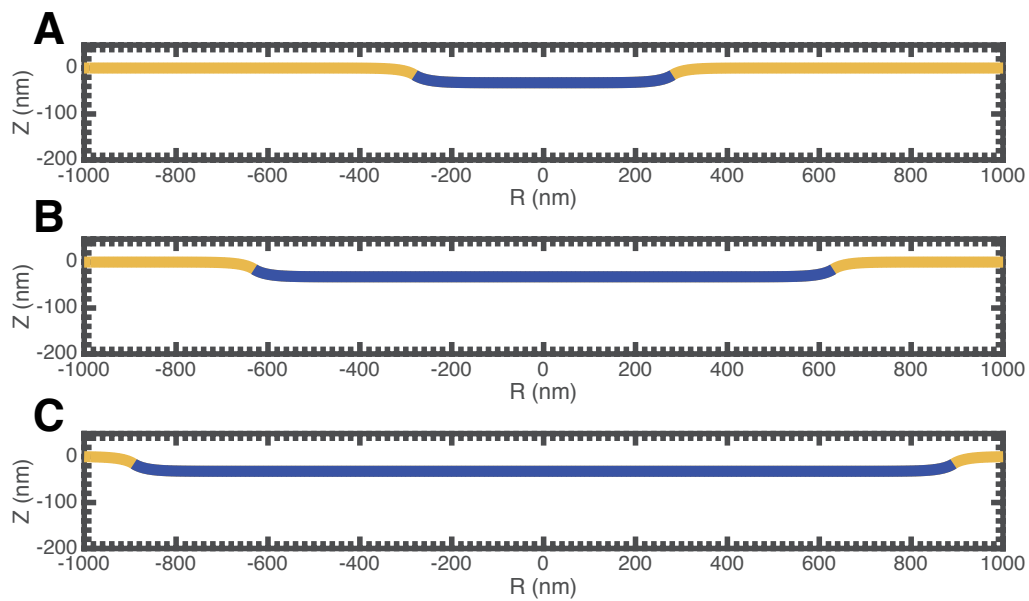


Figure S3: High membrane tension,  $\lambda_0 = 0.2 \text{ pN/nm}$ ,  $C_0 = 0.02 \text{ nm}^{-1}$ . At high membrane tension, the coat can grow arbitrarily large without causing a substantial deformation of the membrane. (A)  $A_{\text{coat}} = 251,327 \text{ nm}^2$ , (B)  $A_{\text{coat}} = 1,256,637 \text{ nm}^2$ , (C)  $A_{\text{coat}} = 2,513,274 \text{ nm}^2$



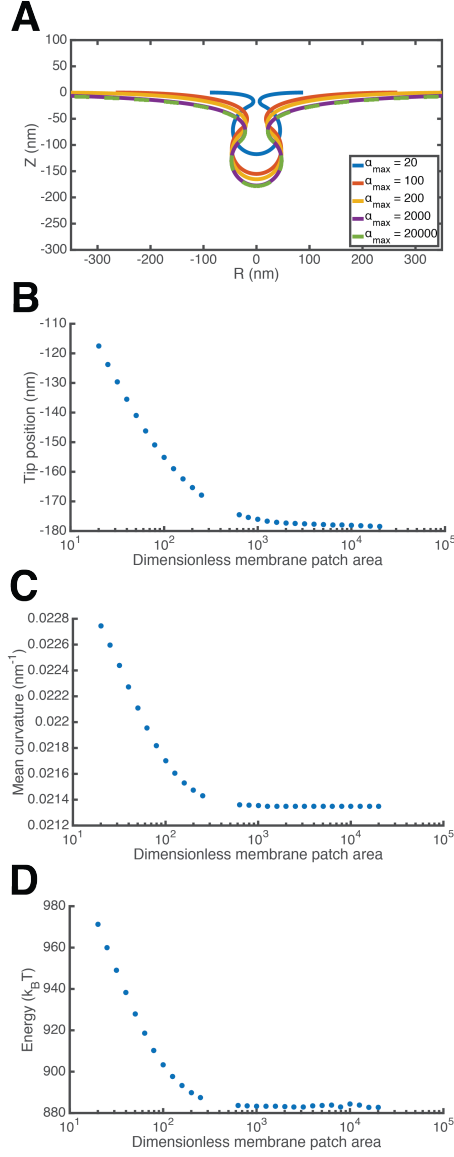


Figure S4: The size of the membrane patch has essentially no effect on the observed deformations of the membrane as long as it is sufficiently large. **(A)** Membrane profiles for identical coat areas and differing total patch areas.  $\lambda_0 = 0.002$  pN/nm,  $A_{\text{coat}} = 25,133$  nm<sup>2</sup>,  $C_0 = 0.02$  nm<sup>-1</sup>. The deformations are identical for very large membrane patches. **(B-D)** Z-position of the bud tip, mean curvature of the bud tip, and energy to deform the membrane, respectively, as a function of the dimensionless area of the membrane patch. The deformation of the membrane is sensitive to small membrane patches, but is essentially identical beyond  $\alpha_{\max} \approx 200$ , particularly in terms of the tip mean curvature and the deformation energy.

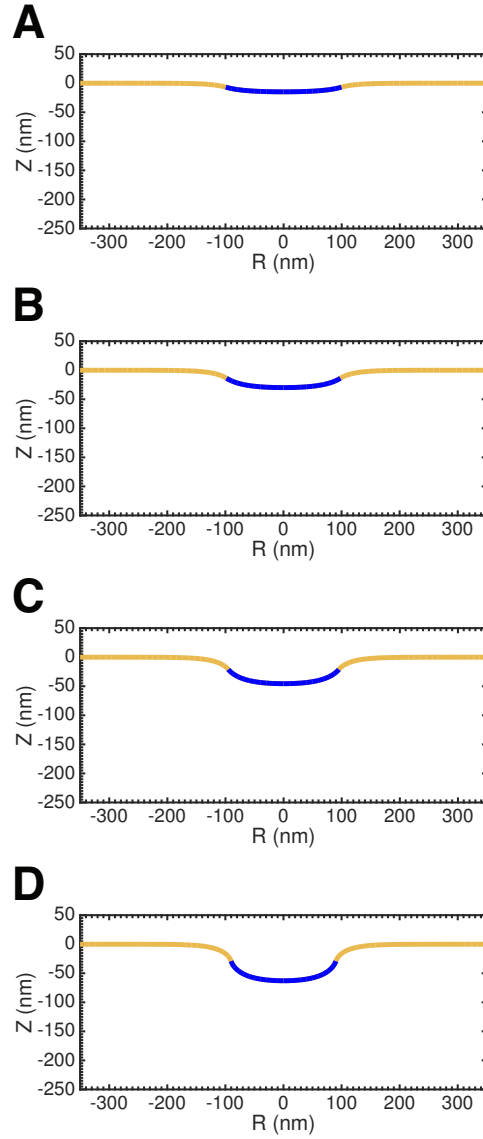


Figure S5: Increasing the spontaneous curvature of the coat at high membrane tensions does not produce closed buds.  $A_{\text{coat}} = 31,416 \text{ nm}^2$ ,  $\lambda_0 = 0.2 \text{ pN/nm}$ . (A)  $C_0 = 0.01 \text{ nm}^{-1}$  (B)  $C_0 = 0.02 \text{ nm}^{-1}$  (C)  $C_0 = 0.03 \text{ nm}^{-1}$  (D)  $C_0 = 0.04 \text{ nm}^{-1}$

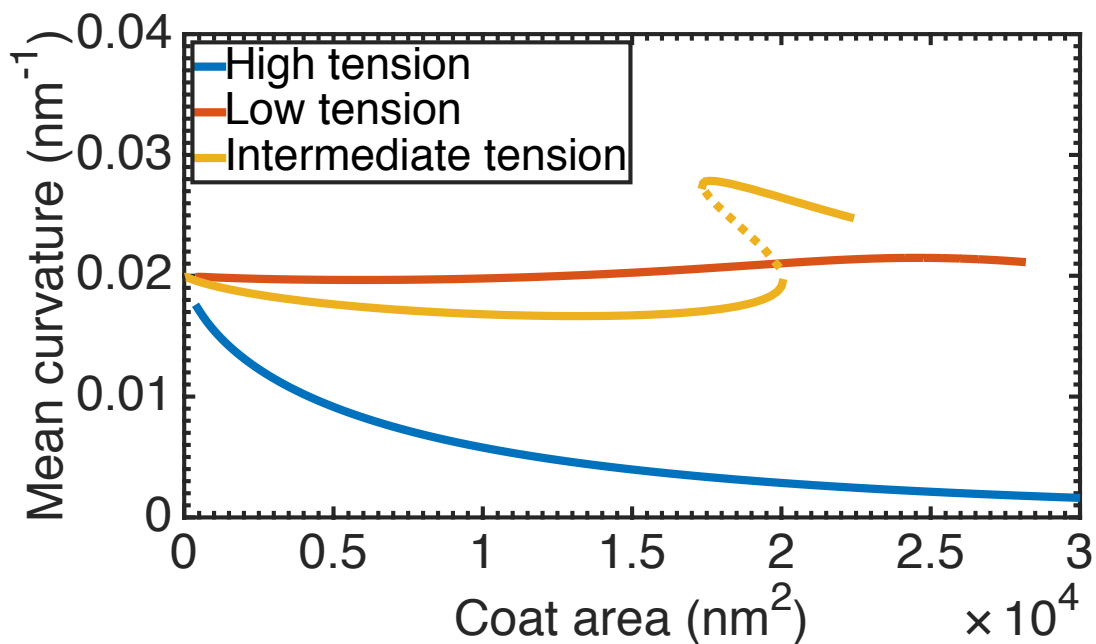


Figure S6: Mean curvature at the bud tip as a function of the area of the coat for the three different membrane tension cases. **High membrane tension**,  $\lambda_0 = 0.2$  pN/nm: The mean curvature at the bud tip drops to nearly  $0 \text{ nm}^{-1}$  as the size of the coat increases and the membrane stays essentially flat at the center of the patch (Figure 2A-C). **Low membrane tension**,  $\lambda_0 = 0.002$  pN/nm: The mean curvature at the bud tip remains at approximately  $0.02 \text{ nm}^{-1}$  as the size of the coat increases and the membrane adopts the spontaneous curvature of the coat (Figure 2D-F). **Intermediate membrane tension**,  $\lambda_0 = 0.002$  pN/nm: Reproduced from Figure 4B. The mean curvature at the bud tip is lower for open buds (lower solution branch) relative to the low tension case, indicating that tension is inhibiting curvature generation by the coat. In contrast, the curvature is higher in the closed buds (upper solution branch) relative to closed buds in the low tension case, showing that membrane tension serves to shrink the size (and hence increase the curvature) of closed buds.

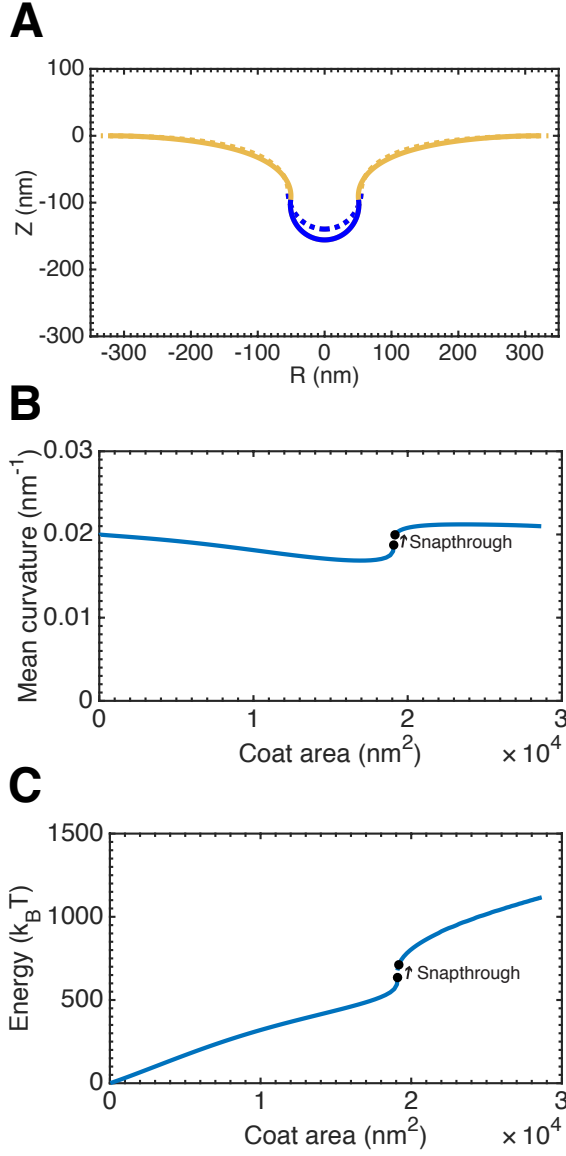


Figure S7: A snapthrough instability is present with increased coat stiffness when progressively increasing the coat area at intermediate membrane tension,  $\lambda_0 = 0.02 \text{ pN/nm}$ . The coat stiffness was increased to  $k_{\text{coat}} = 2400 \text{ pN} \cdot \text{nm} \approx 300 k_B T$  [46], while maintaining uncoated membrane stiffness at  $k_{\text{coat}} = 320 \text{ pN} \cdot \text{nm} \approx 80 k_B T$ . (A) Membrane profile showing the morphology before (dashed line,  $A_{\text{coat}} = 19,083 \text{ nm}^2$ ) and after (solid line,  $A_{\text{coat}} = 19,171 \text{ nm}^2$ ) a small addition of area to the coat. (B-C) Mean curvature at the tip of the bud and energy necessary to deform the membrane as a function of the area of the coat. A snapthrough instability is present with a stiffer coat, though the energy difference between the U- and  $\Omega$ -shaped pits is only  $\approx 75 k_B T$  and the solution branches overlap very slightly.

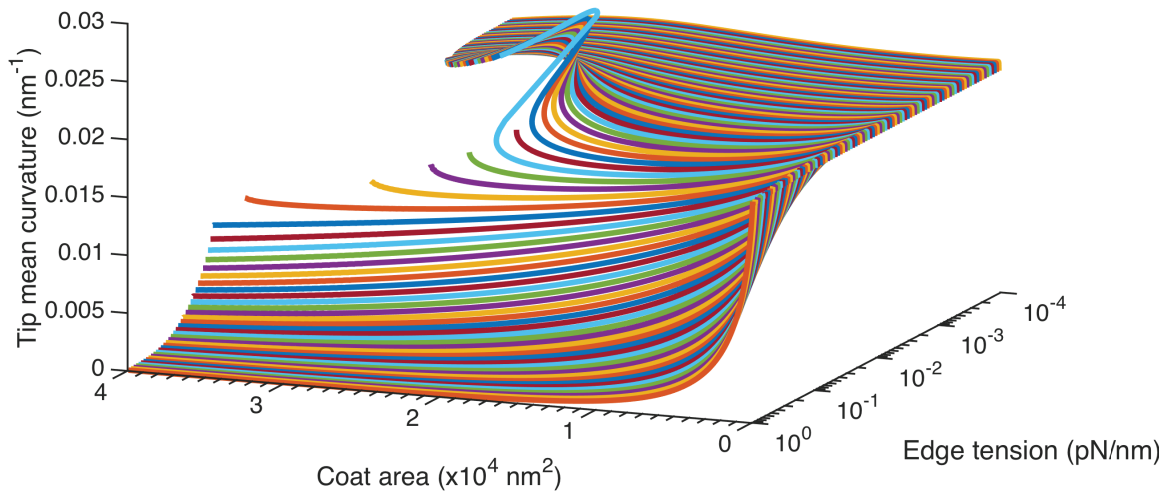


Figure S8: Cusp catastrophe surface. The mean curvature at the tip of the bud is plotted as a function of the membrane tension and coat area. Membrane tension is on a log scale. Three regimes exist: 1) Low tension: The membrane smoothly evolves from flat to a closed bud. The tip mean curvature remains nearly constant at the preferred curvature of the coat. 2) High tension: The membrane remains nearly flat as the coat area increases. The tip mean curvature goes to zero as the size of the coat increases. 3) Intermediate tension: A snapthrough instability in the tip mean curvature exists after a bifurcation point is reached.

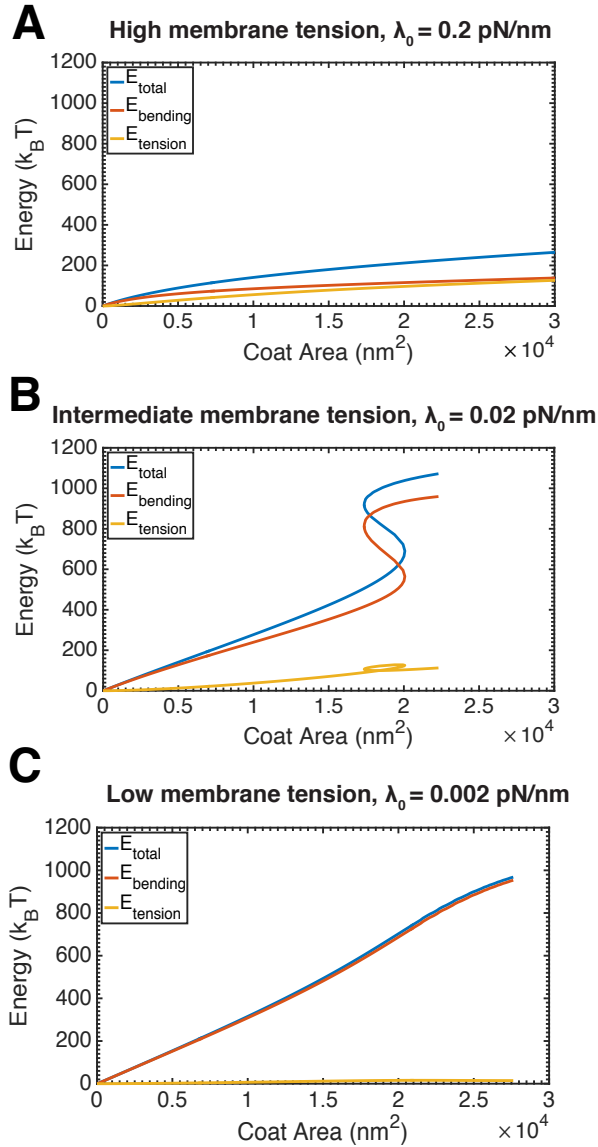


Figure S9: Energy to deform the membrane as a function of the coat area. **(A)** High membrane tension,  $\lambda_0 = 0.2$  pN/nm: There is no substantial deformation of the membrane at high tensions by the coat, and so the total work done to deform the membrane is relatively low. The work done against bending rigidity and against tension are of the same order of magnitude. **(B)** Intermediate membrane tension,  $\lambda_0 = 0.02$  pN/nm: The main contribution to the deformation energy is work done against bending rigidity. Importantly, the energy barrier between open and closed bud morphologies is still present in the work done against bending rigidity and is not just a consequence of work done against the membrane tension. **(C)** Low membrane tension,  $\lambda_0 = 0.002$  pN/nm: Nearly all of the work done is against bending rigidity.

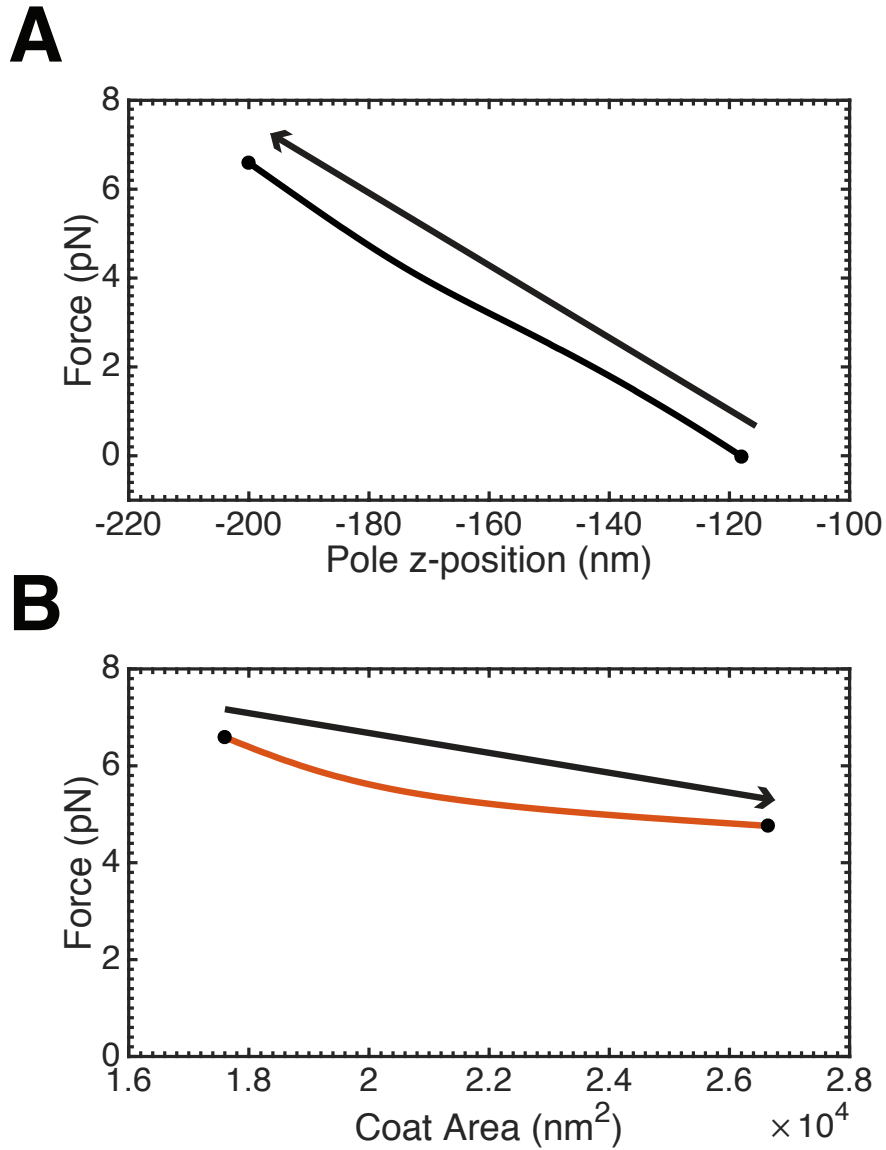


Figure S10: Pulling force simulations. **(A)** Applied force as a function of the z-position of the bud tip. The arrow denotes the direction of the simulation with the marked points denoting the solutions depicted in Figure 8A. The applied force necessary to hold the bud at the prescribed depth increases approximately linearly with increasing depth. **(B)** Applied force as a function of the area of the coat. The arrow denotes the direction of the simulation with the marked points denoting the solutions depicted in Figure 8B. The force necessary to hold the bud tip at  $Z = -200$  nm decreases slightly with increasing coat area.

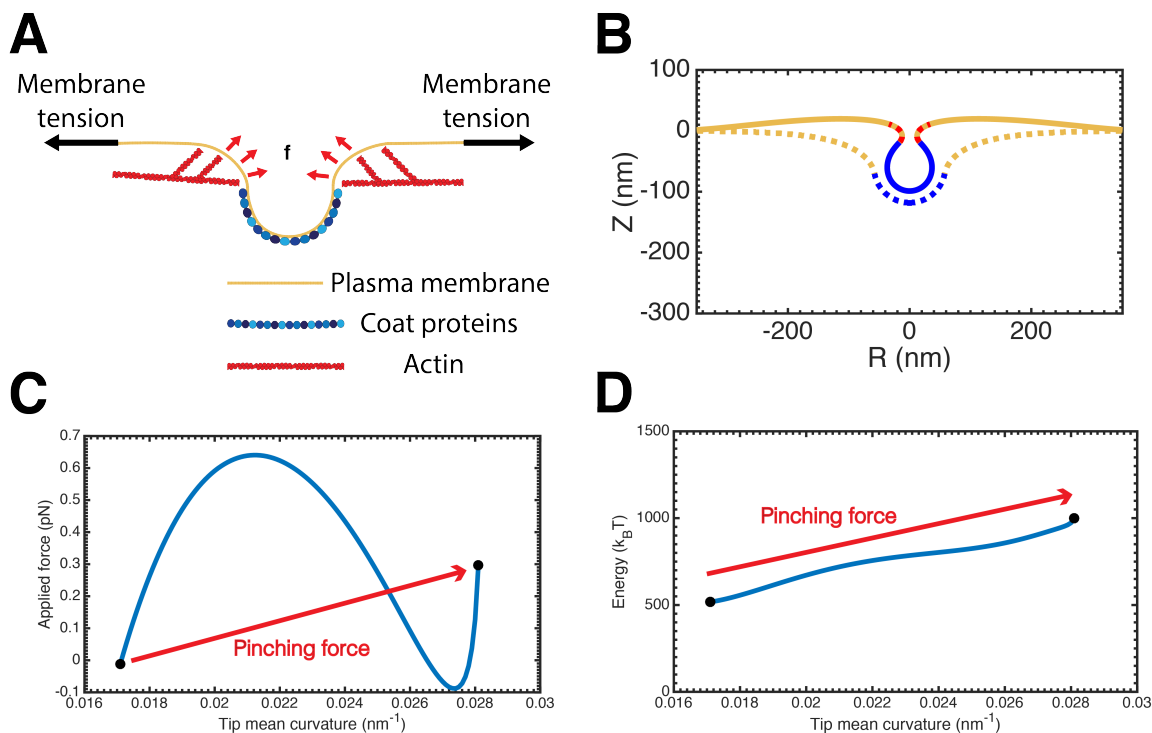


Figure S11: A pinching force can mediate the transition from a U- to  $\Omega$ -shaped bud. The actin force is oriented normal to the membrane in a “collar” situated immediately next to the coated region. **(A)** Schematic showing the orientation and location of the pinching force. **(B)** Profile view showing the shape of the membrane before (dashed line) and after (solid line) application of a pinching force at constant coat area,  $A_{\text{coat}} = 17,593 \text{ nm}^2$ . **(C)** Total applied force as a function of the mean curvature at the tip of the bud. The force remains below 1 pN, well within the capability of a few actin filaments [48]. **(D)** Energy necessary to deform the membrane as a function of the mean curvature at the tip of the bud. Approximately  $500 k_B T$  is necessary to deform the membrane from the open U-shape to the closed  $\Omega$ -shape as depicted in (B), well within the capability of a few hundred actin monomers assuming a  $\approx 5\%$  energy efficiency [48].